
EFFICIENT BAYESIAN TRAVEL-TIME TOMOGRAPHY WITH GEOLOGICALLY-COMPLEX PRIORS USING SENSITIVITY-INFORMED POLYNOMIAL CHAOS EXPANSION AND DEEP GENERATIVE NETWORKS

A PREPRINT

Giovanni Angelo Meles
Institute of Earth Sciences
University of Lausanne
Switzerland
Giovanni.Meles@unil.ch

Macarena Amaya
Institute of Earth Sciences
University of Lausanne
Switzerland
Macarena.Amaya@unil.ch

Shiran Levy
Institute of Earth Sciences
University of Lausanne
Switzerland
Shiran.Levy@unil.ch

Stefano Marelli
Institute of Structural Engineering
ETH Zurich
Switzerland
Marelli@ibk.baug.ethz.ch

Niklas Linde
Institute of Earth Sciences
University of Lausanne
Switzerland
Niklas.Linde@unil.ch

July 20, 2023

ABSTRACT

Monte Carlo Markov Chain (MCMC) methods commonly confront two fundamental challenges: accurate characterization of prior distributions and efficient evaluation of likelihoods. In the context of Bayesian studies on tomography, principal component analysis (PCA) can in some cases facilitate the straightforward definition of the prior distribution, while simultaneously enabling the implementation of accurate surrogate models based on polynomial chaos expansion (PCE) to replace computationally intensive full-physics forward solvers. When faced with scenarios where PCA does not offer a direct means of easily defining the prior distribution alternative methods like deep generative models (e.g., variational autoencoders (VAEs)), can be employed as viable options. By sampling a simple prior probability distribution defined in the low-dimensional latent space of a VAE, it becomes possible to efficiently sample the physical domain. This is accomplished by employing a generator that is typically highly non-linear. Deep generative models therefore offer appealing features for MCMC. However, accurately producing a surrogate capable of capturing the intricate non-linear relationship between the latent parameters of a VAE and the outputs of forward modeling presents a notable challenge. Indeed, while PCE models provide high accuracy when the input-output relationship can be effectively approximated by relatively low-degree multivariate polynomials, this condition is typically unmet when utilizing latent variables derived from deep generative models. In this contribution, we present a strategy that combines the excellent reconstruction performances of VAE in terms of prior representation with the accuracy of PCA-PCE surrogate modeling in the context of Bayesian ground penetrating radar (GPR) travel-time tomography. Within the MCMC process, the parametrization of the VAE is leveraged for prior exploration and sample proposal. Concurrently, modeling is conducted using PCE, which operates on either globally or locally defined principal components of the VAE samples under examination. Our methodology is exemplified using channelized subsurface structures, providing accurate reconstructions and significant speed-ups, particularly in cases where the computation of the full-physics forward model is costly.

1 Introduction

Bayesian inversion methods can account for data and modeling uncertainties as well as prior knowledge, thus, representing an attractive approach for tomography. However, the difficulties in specifying appropriate prior distributions and high computational burden associated with repeated forward model evaluations often hinder proper implementation of Bayesian tomography (Chipman et al., 2001) or make it computationally very expensive. In geophysical settings, prior distributions have traditionally been specified by assuming the subsurface to be represented by a Gaussian random field. As an alternative, in cases where this assumption is invalid, the prior can be informed using training images (TI), that is, large gridded 2-D or 3-D unconditional representations of the expected target spatial field that can be either continuous or categorical (Mariethoz and Caers, 2014; Laloy et al., 2017, 2018). Proper parametrization of the prior is essential in Bayesian inversion, and the most suitable prior parametrization may differ from what is commonly used for other purposes. For example, in physics-based modeling and visualization, representations of geophysical media most often rely on pixel-based parametrizations. Physical media can then be associated with points in \mathbb{R}^N , where N is the number of elements in the corresponding pixel-based representation. However, while allowing easy implementation of forward modeling schemes (e.g., Finite Difference (FD) based on partial differential equations), pixel-based N -dimensional parametrizations are often not suitable to effectively parametrize the prior distribution, as N can be very large. When prior knowledge implies that the spatial patterns are constrained (e.g., in terms of covariance or connected spatial structures), the prior-compatible models populate manifolds embedded in \mathbb{R}^N . If this manifold can be locally assimilated to a subset of \mathbb{R}^M , with $M \ll N$, the prior distribution reduces to a function of M variables only, which leads to lower-dimensional inverse problems.

Manifold identification for Bayesian methods through dimensionality reduction can be accomplished using various approaches, with principal component analysis (PCA) and related methods being the most widely used linear dimensionality reduction techniques (Boutsidis et al., 2008; Jolliffe and Cadima, 2016). Based on a data set of prior model realizations and the eigenvalues/eigenvectors of the corresponding covariance matrix, PCA provides optimal M -dimensional representations in terms of uncorrelated variables that retain as much of the sample variance as possible. The dimensionality reduction is achieved by projecting data on the first M eigenvectors (or principal components) sorted according to the descending order of the relative eigenvalues. PCA has found widespread application in geophysics, utilized in both deterministic and stochastic inversion algorithms, with recent advancements in this field offering the potential to reconstruct even discontinuous structures (Reynolds et al., 1996; Giannakis et al., 2021; Meles et al., 2022; Thibaut et al., 2021). In the context of media characterized by binary, channelized aquifer structures, which has been explored by several authors (Strebelle, 2002; Zahner et al., 2016; Laloy et al., 2018) and investigated in this study, PCA-based methods may however encounter challenges in identifying a lower-dimensional manifold that is suitable for easy sampling, which is particularly desirable in MCMC methods. As an effective alternative, deep generative models such as variational autoencoders (VAEs) or Spatial Generative Adversarial Networks (SGANs) can be employed to achieve a low-dimensional parameterization of complex media distributions, facilitating easy sampling. VAEs and SGANs are distinct types of deep generative models, both utilizing deep neural networks to learn the underlying input distribution and generate synthetic samples that closely resemble a provided dataset. VAEs capture patterns in data through a compressed latent space for reconstruction and generation. SGANs use adversarial training to generate realistic synthetic output resembling reference data (Kingma and Welling, 2013; Jetchev et al., 2016; Goodfellow et al., 2020). In this manuscript we use VAEs since it was recently suggested that their lower degree of nonlinearity in the corresponding networks makes them more amenable for inversion (Lopez-Alvis et al., 2021; Levy et al., 2022b). For the purpose of Bayesian inversion, VAEs possess a crucial property: they generate realizations that exhibit patterns consistent with the TI when applied to random realizations drawn from an uncorrelated standard normal or uniform distribution (Laloy et al., 2017). The presence of a low-dimensional parameterization representing the prior distribution simplifies the sampling process, making it well-suited for Markov chain Monte Carlo (MCMC) schemes. However, employing a VAE parameterization does not in any way alleviate the challenge of computational load associated with MCMC methods, which can be substantial in applications like ground-penetrating radar (GPR) travel-time tomography. Travel-time tomography refers to various imaging methods where the propagation of acoustic, elastic or electro-magnetic waves is used to non-destructively infer media properties. Applications range from seismology (Rawlinson et al., 2003) to natural resources exploration (Taillandier et al., 2009), atmosphere temperature and wind velocity estimates (Vecherin et al., 2006), medical investigations (Semenov, 2009) and non-destructive testing (Tant et al., 2018). High-resolution MCMC travel-time tomography of electromagnetic ground wave velocity distribution in the shallow subsurface can be performed using ground-penetrating radar (GPR). GPR wave-propagation is governed by the distribution of dielectric permittivity (ϵ) and electric conductivity (σ) in the subsurface. However, wave propagation velocity mainly depends on permittivity, which is in turn related to porosity and water content through petrophysical relationships (Gloaguen et al., 2005). GPR data can be collected in a variety of configurations, with cross-hole designs being particularly well suited for groundwater investigations (LaBrecque et al., 2002; Annan, 2005). Deterministic and probabilistic algorithms alike have been proposed for the inversion of GPR data, either by considering the travel-time and/or amplitude of the

first-arrival signals (Olsson et al., 1992) or the waveforms of the measured electromagnetic fields (Ernst et al., 2007; Kuroda et al., 2007; Meles et al., 2010; ?; Klotzsche et al., 2019).

When MCMC schemes are used for GPR travel-time inversion, the high computational cost associated with the many (often hundreds of thousands or millions) forward model evaluations required to locate and sample from the posterior distribution can be computationally prohibitive, even if state-of-the-art FD solvers are used (Warren et al., 2019). Consequently, it is important to find ways to speed-up the forward calculations. Machine learning (ML) and deep neural network (DNN) tools have become increasingly popular in recent years, rivaling physics-based solvers in many applications by providing inexpensive proxies mimicking the non-linear input-output relations of standard forward solvers. Neural network-based inversion strategies have already been used for various global search GPR inversion algorithms (Hansen and Cordua, 2017; Giannakis et al., 2019). Even if surrogate modeling with DNNs is very promising and topical, polynomial chaos expansion (PCE) surrogate models (Xiu and Karniadakis, 2002; Blatman and Sudret, 2011) may still be highly competitive, particularly as there is less need for training data. PCEs have already been massively employed in Bayesian inverse problems (Nagel, 2019; Higdon et al., 2015; Marzouk and Xiu, 2009; Marzouk et al., 2007; Wagner et al., 2020, 2021a). For Bayesian travel-time tomography, a pioneering use of PCE surrogates for 1.5D settings was introduced by Sochala et al. (2021). More recently, Meles et al. (2022) proposed a Bayesian framework based on PCEs operating on data-driven PCs to model GPR travel-time and perform tomography with 2D multi-Gaussian priors. A multivariate polynomial of maximum degree equal to 5 lead to modeling errors that were significantly smaller than the expected noise level and, therefore, resulted in successful Bayesian inversion. It was also shown that the modeling error resulting from using the PCE surrogate is approximately Gaussian and largely uncorrelated, making it much easier to include in the inversion than if using a surrogate based on simplified physics (Levy et al., 2022a).

Given these considerations, one might speculate that for tomography of media characterized by binary, channelized structures combining a VAE parametrization within PCE modeling would effectively address both issues simultaneously. This idea aligns with the findings presented in Meles et al. (2022), where a similar approach was employed, albeit with PCA decomposition. However, our contribution contradicts this speculation and demonstrates that in this case utilizing a VAE parametrization for both the prior and PCE modeling leads to sub-optimal outcomes. As alternatives, to exploit the advantageous features of both VAEs and PCE, we propose the separation of input parametrization between the inversion and modeling steps. In this approach, we utilize the latent representation to define the prior distribution and explore the posterior distribution. Simultaneously, we rely on either global or local sensitivity kernel-based PCA decompositions of the input generated by the underlying VAE decoder to facilitate the modeling process and show how to account for the intrinsic difficulties of PCE to handle high dimensional input.

Numerical examples validate the efficacy of the proposed strategy, effectively combining the capability to handle complex geological priors enabled by a VAE parametrization with the computational efficiency and high accuracy afforded by PCE-based forward modeling.

2 Methodology

2.1 Bayesian inversion

Forward models are mathematical tools that quantitatively evaluate the outcome of physical experiments. We refer to the relationship between input parameters and output values as the 'forward problem':

$$\mathcal{F}(\mathbf{u}) = \mathbf{y} + \epsilon. \quad (1)$$

Here, \mathcal{F} , \mathbf{u} , \mathbf{y} and ϵ stand for the physical law or forward operator, the input parameters, typically representing local media properties, the output and a noise term, respectively. The goal of the 'inverse problem' associated with the 'forward problem' in Eq. (1) is to infer properties of \mathbf{u} conditioned by the data \mathbf{y} while taking into account any available prior information about \mathbf{u} . A general solution to this problem can be expressed in terms of the posterior distribution defined over the input domain by Bayes' theorem:

$$P(\mathbf{u}|\mathbf{y}) = \frac{P(\mathbf{y}|\mathbf{u})P(\mathbf{u})}{P(\mathbf{y})} = \frac{L(\mathbf{u})P(\mathbf{u})}{P(\mathbf{y})}. \quad (2)$$

Here, $P(\mathbf{u}|\mathbf{y})$ is the posterior distribution of the input parameter \mathbf{u} given the data \mathbf{y} , $P(\mathbf{y}|\mathbf{u})$ (also indicated as $L(\mathbf{u})$ and known as 'the likelihood') is the probability of observing the data \mathbf{y} given the input parameter \mathbf{u} , while $P(\mathbf{u})$ and $P(\mathbf{y})$ are the prior distribution in the input parameter domain and the marginalized likelihood with respect to the input parameters (also known as evidence), respectively. In practical applications, Eq. (2) is seldom used when solving inverse problems as the computation of the evidence is in most cases very expensive. However, since the numerator of the right-hand side of Eq. (2), that is, $L(\mathbf{u})P(\mathbf{u})$, is proportional to the posterior distribution, one can use a Markov

chain Monte Carlo (MCMC) methods to draw samples proportionally from $P(\mathbf{u}|\mathbf{y})$ without considering the evidence (Hastings, 1970). For practical applications, computation of both $P(\mathbf{u})$ and $L(\mathbf{u})$ is often critical. Evaluation of $P(\mathbf{u})$ can be expensive for high-dimensional problems. This is the case for tomography, where \mathbf{u} typically represents the slowness distribution at every point/pixel in space. Moreover, computing $L(\mathbf{u})$ requires the solution of a forward problem, which can be extremely demanding in Bayesian scenarios as this evaluation needs to be repeated many times. In the following sections we discuss how both these problems can be approached by using a latent representation and surrogate modeling to evaluate $P(\mathbf{u})$ and $L(\mathbf{u})$, respectively.

2.2 Dimensionality reduction for Bayesian inversion and forward modeling

Sets of parameters are particularly well suited for Bayesian inversion accelerated by surrogate modeling when they can easily encode the prior distribution and represent the physics of the problem under investigation (Meles et al., 2022). Meles et al. (2022) used variables defined in terms of principal components to (a) represent the prior distribution related to a random Gaussian field on a low-dimensional manifold *and* (b) implement an accurate surrogate to compute the forward problem. However, it is not generally granted that a single change of coordinates can achieve both (a) and (b). We first focus on (a), that is, the proper representation of the prior on a low-dimensional manifold. For the representation of the prior, here informed using TI, we consider coordinates \mathbf{z} induced by a VAE deep generative network \mathcal{G}_{VAE} mapping the latent space into the physical one, that is: $\mathcal{G}_{VAE}(\mathbf{z}) = \mathbf{u}$. The details of the decoder utilized in this study can be found in (Laloy et al., 2017). The use of this new set of coordinates \mathbf{z} casts the inverse problem on the latent manifold as:

$$P(\mathbf{z}|\mathbf{y}) = \frac{P(\mathbf{y}|\mathbf{z})P(\mathbf{z})}{P(\mathbf{y})}. \quad (3)$$

While formally identical to Eq. (2), Eq. (3) involve significant advantages. For this class of coordinates, not only \mathbf{z} is typically low-dimensional (i.e., at most up to few tens of variables), but the corresponding statistical prior distribution $P(\mathbf{z})$ can be designed to be a multivariate standard Gaussian distribution during VAE training. For the sake of discussing (b), we now rewrite the forward problem in Eq. (1) using the new coordinates:

$$\mathcal{N}_{VAE}(\mathbf{z}) = \mathbf{y} + \epsilon, \quad (4)$$

where $\mathcal{N} = \mathcal{F} \circ \mathcal{G}_{VAE}$, \circ stands for function composition, and we assume no error induced by the VAE dimensionality reduction. Due to the complexity and non-linearity of \mathcal{G}_{VAE} , we can expect the forward operator \mathcal{N} to be highly irregular. As detailed in section 2.3 and 4, the complexity of \mathcal{N}_{VAE} can be problematic for (b), i.e., the implementation of surrogate modeling, which can lead to poor MCMC performances. The adherence to the latent parametrization is motivated by its pivotal capability to capture complex priors. However, it becomes necessary to explore alternative approaches in order to construct an accurate surrogate model that circumvents the use of the latent parametrization. In the next sections, we demonstrate the potential of incorporating an additional changes of coordinates through the application of PCA. However, it is important to note that this utilization of PCA is solely restricted to the modeling aspect, which differs from the approach discussed in Meles et al. (2022). For the problem at hand, the use of PCA presents a critical challenge in generating realizations consistent with the TI. Nonetheless, our study highlights that PCA still possesses desirable properties that contribute to its value in modeling, even within this particular scenario.

By considering a complete set of principal components for realizations of the deep generative network (implemented via $\mathcal{G}_{PCA}(\mathbf{x}_{full}) = \mathcal{G}_{VAE}(\mathbf{z}) = \mathbf{u}$) we can rewrite Eq. (1) as:

$$\mathcal{M}_{PCA}(\mathbf{x}_{full}) = \mathbf{y} + \epsilon, \quad (5)$$

where $\mathcal{M}_{PCA} = \mathcal{F} \circ \mathcal{G}_{PCA}$. We show in the following that the relatively simple relationship $\mathcal{G}_{PCA}(\mathbf{x}_{full}) = \mathbf{u}$ makes it suitable for implementing a surrogate of \mathcal{M}_{PCA} , provided that the input and the model can be faithfully represented as operating on an effective M -dimensional truncated subset \mathbf{x} of the new coordinates \mathbf{x}_{full} , that is: $\mathcal{G}_{PCA}(\mathbf{x}) \approx \mathbf{u}$ and

$$\mathcal{M}_{PCA}(\mathbf{x}) = \mathbf{y} + \hat{\epsilon}, \quad (6)$$

where $\hat{\epsilon}$ is a term including both observational noise and modeling errors related to the projection on the subset represented by \mathbf{x} .

Once a suitable prior has been defined *and* a accurate modeling strategy devised, in our case based on VAE *and* principal components parametrizations, respectively, a Metropolis-Hastings MCMC algorithm can be used to sample the posterior distribution $P(\mathbf{z}|\mathbf{y})$ (Hastings, 1970). A sample of the posterior in the physical space, $P(\mathcal{G}_{VAE}(\mathbf{z})|\mathbf{y})$, is then also available via mere application of the \mathcal{G}_{VAE} to draws from $P(\mathbf{z}|\mathbf{y})$. The latent representation provided by the VAE is used to evaluate $P(\mathbf{z})$ and explore the posterior according to a Gaussian proposal distribution characterized by a diagonal covariance matrix $\lambda\mathbb{I}$, where λ can be tuned to achieve a proper acceptance rate (Marelli and Sudret, 2014; Meles et al., 2022). For each step in the MCMC process, the surrogate modeling operates on subsets \mathbf{x} of principal components associated with the physical distribution $\mathcal{G}_{VAE}(\mathbf{z})$ proposed by the MCMC.

2.3 Polynomial chaos expansion

Forward models are typically implemented by potentially expensive schemes (e.g. finite element methods, Finite-Difference Time-Domain (FDTD)) that solves physical equations to mimic the relationship between input and output data. As discussed in section 2.2, the function a forward solver has to model depends on the set of coordinates used to represent the input. For simplicity, we focus here on the derivation of a surrogate for $\mathcal{M}_{PCA}(\mathbf{x})$, but identical formal derivations would apply to \mathcal{N}_{VAE} or \mathcal{F} , albeit with relevant caveats that will be discussed below. A surrogate model $\tilde{\mathcal{M}}_{PCA}$ is a function that seeks to emulate the behaviour of an expensive forward model at negligible computational cost per run:

$$\tilde{\mathcal{M}}_{PCA}(\mathbf{x}) \approx \mathcal{M}_{PCA}(\mathbf{x}). \quad (7)$$

Among the many available surrogate models, sparse adaptive polynomial chaos expansions are one of the most widely used due to their efficiency, flexibility and ease of deployment (Xiu and Karniadakis, 2002; Blatman and Sudret, 2011; Lüthen et al., 2021b; Métivier et al., 2020). Polynomial chaos expansions are a type of stochastic spectral expansions that can approximate forward operators in terms of linear combinations of orthonormal multivariate polynomials Ψ_α :

$$\tilde{\mathcal{M}}_{PCA}(\mathbf{x}) = \sum_{\alpha \in \mathcal{A}} a_\alpha \Psi_\alpha(\mathbf{x}), \quad (8)$$

where M is the dimension of \mathbf{x} and \mathcal{A} is a subset of \mathbb{N}^M implementing a truncation scheme to be set based on accuracy requirements and computational resources availability (Xiu and Karniadakis, 2002). For a review of more advanced basis truncation and construction schemes, the reader is redirected to Lüthen et al. (2021a). To calculate the set of expansion coefficients a_α sparse regression techniques, also known as compressive sensing, have been demonstrated to be highly efficient in the context of surrogate modeling (Torre et al., 2019; Lüthen et al., 2021b,a), and are adopted in this paper. Note that the evaluation of the coefficients a_α is computationally unfeasible when the input domain is high-dimensional (the case for a surrogate $\tilde{\mathcal{F}}(\mathbf{u})$ of $\mathcal{F}(\mathbf{u})$). Moreover, when the truncation pattern cannot fully account for the degree of non-linearity of the underlying model (the case for a surrogate $\tilde{\mathcal{N}}_{VAE}(\mathbf{z})$ of $\mathcal{N}_{VAE}(\mathbf{z})$), the still unbiased PCE predictions are inevitably affected even if the input domain is low-dimensional. In any case, if a_α is calculated from a finite data set, the surrogate forward modeling predictor can be evaluated at a negligible cost by direct computation of Eq. (8) and its accuracy estimated using a validation set or cross-validation techniques (Blatman and Sudret, 2011; Marelli et al., 2021). In this manuscript, we focus on PCE surrogates operating on latent variables (i.e., $\tilde{\mathcal{N}}_{VAE}(\mathbf{z})$) and principal components (i.e., $\tilde{\mathcal{M}}_{PCA}(\mathbf{x})$).

3 Modeling-error aware likelihood function

A PCE surrogate model can be used to predict physical quantities such as \mathbf{y} in Eq. (6). Since we rely on an imperfect surrogate model operating on a truncated domain it is important to incorporate the corresponding modeling error in the inversion process by using an appropriate likelihood function. The likelihood function discussed in Section 2.2 is assumed to be Gaussian. We account for the modeling error by considering a covariance operator \mathbf{C}_D given by the sum of the covariance matrices describing data uncertainty, indicated in the following as \mathbf{C}_d , and a modeling term \mathbf{C}_{Tapp} . The covariance operator associated with the modeling error is defined in terms of a misfit matrix \mathbf{D}_e . For an unbiased model, \mathbf{D}_e consists of T realizations of the difference between the exact and the approximate forward responses. In case of biased models, the bias - indicated in the following as \mathbf{d}_d is added to the approximate responses (Hansen et al., 2014; Madsen and Hansen, 2018; Holm-Jensen and Hansen, 2020). The k^{th} column of \mathbf{D}_e is a n -dimensional vector corresponding to the single k^{th} realization of the modeling error, where n is the dimension of the output domain, thus, \mathbf{D}_e is a $n \times T$ matrix. Given the definition above, the covariance operator \mathbf{C}_D is defined as follows:

$$\mathbf{C}_D = \mathbf{C}_d + \mathbf{C}_{Tapp}, \quad (9)$$

where \mathbf{C}_{Tapp} is defined as the $n \times n$ matrix

$$\mathbf{C}_{Tapp} = \frac{1}{N} \mathbf{D}_e \mathbf{D}_e^T. \quad (10)$$

The likelihood incorporating the modeling error is then expressed as

$$L(\mathbf{x}) = \left(\frac{1}{2\pi} \right)^{n/2} |\mathbf{C}_D|^{-1/2} \exp \left[-\frac{1}{2} (\tilde{\mathcal{M}}_{PCA}(\mathbf{x}) + \mathbf{d}_d - \mathbf{y})^T \mathbf{C}_D^{-1} (\tilde{\mathcal{M}}_{PCA}(\mathbf{x}) + \mathbf{d}_d - \mathbf{y}) \right]. \quad (11)$$

where $|\mathbf{C}_D|$ is the determinant of the covariance matrix \mathbf{C}_D (Hansen et al., 2014). In practice, it is convenient to use the training set implicit in the construction of the PCE itself to synthesise the matrix \mathbf{D}_e . The computation of

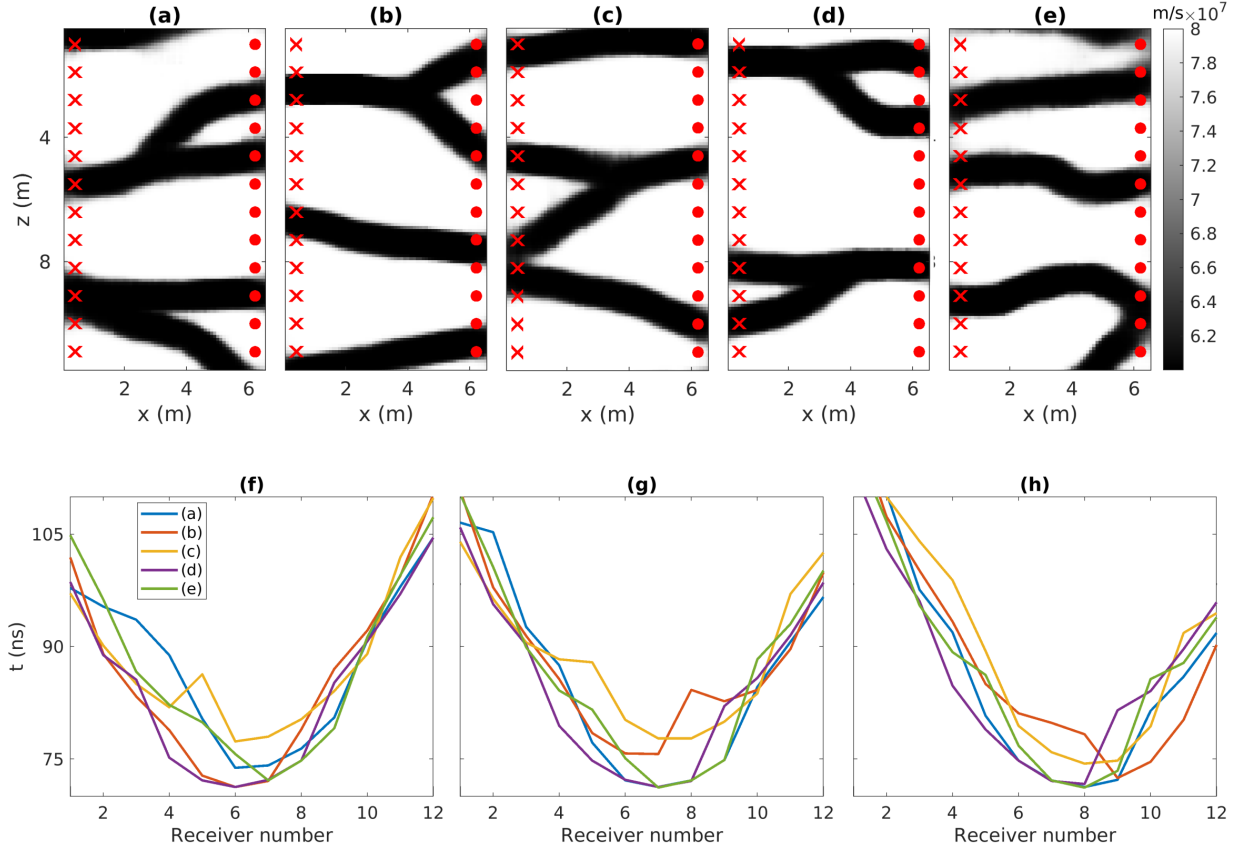


Figure 1: (a-e) Representative velocity distributions as generated by the decoder of the employed VAE; crosses and circles stand for sources and receivers, respectively. (f-h) Corresponding exemplary travel-time gathers.

the k^{th} column of the matrix D_e is defined in terms of the output of the k^{th} element of the training set and a PCE approximation. This PCE estimate is based on cross-validation in which the k^{th} realization is not part of the set used for training. Note that using the surrogate $\tilde{\mathcal{N}}_{VAE}$ in this setting can be made by merely substituting $\tilde{\mathcal{M}}_{PCA}(\mathbf{x})$ with $\tilde{\mathcal{N}}_{VAE}(\mathbf{z})$ and using the corresponding C_D and d_d in Eq. (11).

4 Application to GPR crosshole tomography

In the previous sections, we briefly covered the basic principles of Bayesian methods and emphasized the significance of dimensionality reduction and surrogate models for their implementation. Now, we integrate these concepts to tackle GPR cross-hole travel-time tomography through MCMC. Our focus is twofold: exploring the potential of a VAE architecture to parameterize complex channelized structures in the prior distribution, and investigating the challenges of leveraging PCE for accelerated modeling.

4.1 Input and output for MCMC

For the representation of the prior and posterior exploration in the MCMC process, we consider coordinates induced by a VAE deep generative network \mathcal{G}_{VAE} (Laloy et al., 2017). As for the relevant physical distributions, we target lossless media represented by binary images with two facies of homogeneous GPR velocity ($6 \cdot 10^7$ and $8 \cdot 10^7$ m/s) resembling river channels (Strebelle, 2002; Zahner et al., 2016; Laloy et al., 2018). As for the output, we consider arrival-times associated with the recording configuration displayed in Fig. 1(a-e) with 12 evenly spaced sources and receivers located in two vertically-oriented boreholes. The distance between the boreholes is 4.6 m, while the spacing between sources/receivers is 0.9 m, such that a total of 144 travel-times are collected. We employ both an eikonal and a 2D FDTD solver to simulate noise-free propagation of GPR waves (Irving and Knight, 2006; Hansen et al., 2013).

For the FDTD code each source is characterized by a 100 MHz Blackman–Harris, while perfectly matched layers (PML) surrounding the propagation domain are used to prevent spurious reflections from contaminating the data, while appropriate space-time grids are employed to avoid instability and dispersion artefacts. Travel-times are picked automatically based on a threshold associated with the relative maximum amplitude of each source-receiver pair.

4.2 Parametrization of the input domain for PCE

The utilization of the VAE parametrization allows to faithfully represent complex priors, as demonstrated in Figure 1(a-e). However, the VAE parametrization per se does not alleviate the computational load associated with MCMC methods. As a result, our objective is to develop an efficient and accurate PCE meta-model that can synergistically collaborate with the VAE parametrization.

We propose three different strategies to use PCE in conjunction with the VAE parametrization for prior-sampling, using the complex channelized structures in Zahner et al. (2016) as an example. Note that while we specifically reference a particular case, the proposed strategies have broader applicability and can be utilized in various domains and scenarios. For each strategy we build a corresponding PCE to model travel-time arrivals using the Matlab Package UQlab (Marelli and Sudret, 2014; Marelli et al., 2021). To offer a fair comparison, we employ the same training and validation datasets for all proposed schemes. In the first strategy, referred to as VAE-PCE, the input for the PCE modeling are the 20-dimensional z vectors induced by the VAE deep generative network \mathcal{G} mapping the latent space into the physical one, that is: $\mathcal{G}_{VAE}(z) = \mathbf{u}$ (Lopez-Alvis et al., 2021). The second strategy, in the following Global-PCA-PCE, uses a similar approach to Meles et al. (2022), with inputs of the PCE modeling defined in terms of projections on prior-informed PCA components spanning the entire domain. More specifically, in the Global-PCA-PCE approach we randomly create a total of 1000 slowness realizations $\mathcal{G}_{VAE}(z)$ from the prior and compute the corresponding principal components (see Fig. 2). The input for PCE in the Global-PCA-PCE approach are then the projections of $\mathcal{G}_{VAE}(z)$ on a to-be-chosen number of such PCs. Note that, while following Meles et al. (2022) all PCA processes are defined in terms of slowness, for readability purposes in all of the figures of this manuscript we present velocity fields.

The effective dimensionality of the input with respect to \mathcal{M}_{PCA} , that is, the number of principal components representing the input, is not a-priori defined. Following a similar approach to Meles et al. (2022), the effective dimensionality is here assessed by analysing the convergence to the reference solution in the output domain as a function of the number of principal components. In Fig. 3(a) and (e), two velocity distributions are shown next to the approximate representations (Fig. 3(b-d) and (f)-(h)) obtained by projecting them on 30, 60 and 90 principal components, respectively. As expected, the reconstruction quality improves as more principal components are included.

To quantify the faithfulness of the various reduced parametrizations in terms of the output, we consider 100 realizations of the generative model, and compute the resulting histograms of the travel-time residuals. The root-mean-square error (in the following, rmse) of the misfit between the data associated with the original distribution and its projections on 30, 60 and 90 principal components, shown in Fig. 3(i)-(k), are 1.60, 0.85 and 0.55 ns, respectively, that are to be compared to the expected level of GPR data noise of 1 ns for 100 MHz data (Arcone et al., 1998). The number of principal components required to approximate the forward solver below the expected noise level (i.e., 90 PCs) is larger than discussed in Meles et al. (2022) (i.e., 50 PCs). Building a PCE on such a large basis can be challenging in terms of computational requirements and efficiency, and could lead to poor accuracy if a small training set is employed. To address this, one approach is to either reduce the number of components, which introduces larger modeling errors, or explore alternative parameterizations that offer improved computational efficiency and accuracy. In this study, the Global-PCA-PCE approach utilizes 60 components, while an alternative strategy is developed based on physical considerations to further enhance the modeling process.

A final parametrization can be derived by considering the forward problem’s specific characteristics, which are not taken into account in the aforementioned definition of PCs. In fact, the PCs in the Global-PCA-PCE approach refer to the input field in its entirety. However, the actual arrival-time for a given source/receiver combination depends only on a sub-domain of the entire slowness distribution. This leads us to suggest a local approach, in the following referred to as Local-PCA-PCE. Instead of using principal components describing the entire slowness field, we aim to employ output-driven local principal components that characterize only the sub-domains impacting the physics of the problem (Jensen et al., 2000; Husen and Kissling, 2001). We then expect that fewer local PCs are needed than the global ones to achieve the desired input/output accuracy. In practice, the construction of local PCs involves utilizing fat-ray sensitivity kernels, which capture the sensitivity of arrival-times to small perturbations in the subsurface model, thus providing valuable insights into the regions that have the most significant impact on the observed data. For a given source/receiver pair, the corresponding sensitivity kernel depends on the slowness field itself, with patterns that can vary significantly (see Fig. 4(a)-(j)). The sought local decomposition needs to properly represent any possible slowness field within the prior, thus it reasonable to define it based on a representative sample of input realizations. To reduce the overall PCE computational cost it is also convenient to limit as much as possible the number of used output-driven

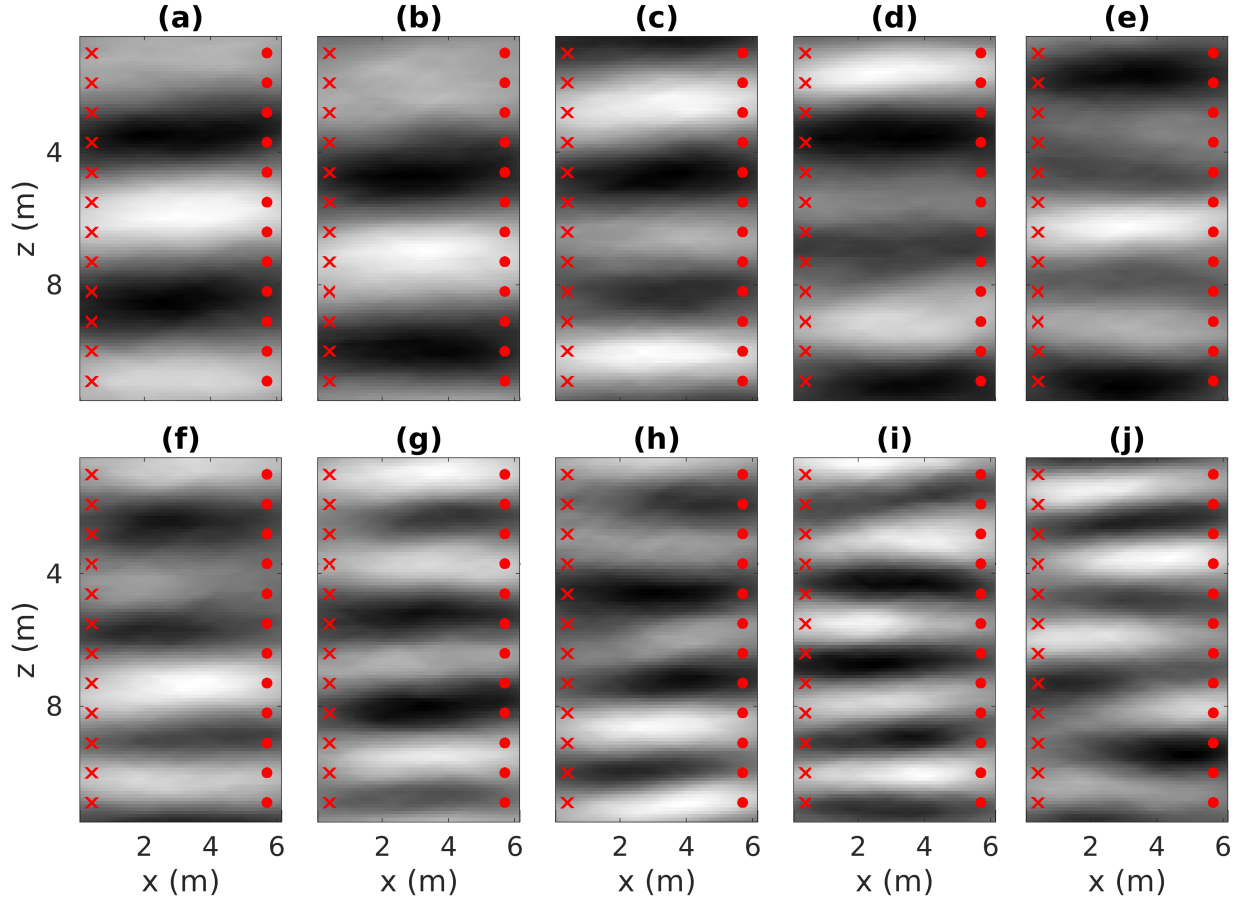


Figure 2: (a-j) The first ten principal components in the input domain corresponding to entire slowness fields. Crosses and circles stand for sources and receivers, respectively.

decompositions. To achieve these goals, we assume that the prior model is stationary with respect to translation. Instead of focusing on each specific source/receiver pair (total number of decompositions in our scenario: 144), we can then consider source/receiver altitude angle (total number of decompositions given our acquisition geometry: 23). We then use a total of 1000 slowness realizations $\mathcal{G}(z)$ from the prior and build the corresponding fat-ray sensitivity kernels using the reference eikonal solver for each of the 23 possible angles (Hansen et al., 2013). For any given angle, we consider a cumulative kernel consisting of the sum of the absolute values of each kernel (green areas in Fig. 4(k)-(t)). Such a cumulative kernel cover an area larger than each individual kernel but is still considerably smaller than the entire slowness field. For any possible additional input model, the corresponding sensitivity kernel is then very likely *geometrically* included in the area covered by the cumulative kernel (see Fig. 4(k)-(t)). Based on this insight, we define principal components spanning only the area covered by such cumulative kernels or relevant parts thereof (e.g., a threshold can be taken into consideration to reduce the size of these sub-domains). For the practical definition of the components, the cumulative kernels are either set to 0 or 1 depending on whether the corresponding value is equal or larger than the threshold, respectively. We then multiply point by point the slowness distributions with the cumulative kernels, and consider the principal components of such products.

In Fig. 5(a)-(e) and (f)-(j), for given source/receiver pairs, the first five principal components are shown. Note that the pattern variability is confined within the cumulative kernels, while in the complementary areas the values are 0. Note also that compared to the first five principal components in Fig. 2, higher resolution details can be identified in the sensitivity confined modes. Given the same number of PCs used, we can then expect the input to be better presented in the physically relevant sub-domain when the Local-PCA-PCE rather than the Global-PCA-PCE approach is followed. For all source/receiver pairs corresponding to the same altitude angle, the same kernels and principal components are used, provided they are shifted to cover the appropriate geometry.

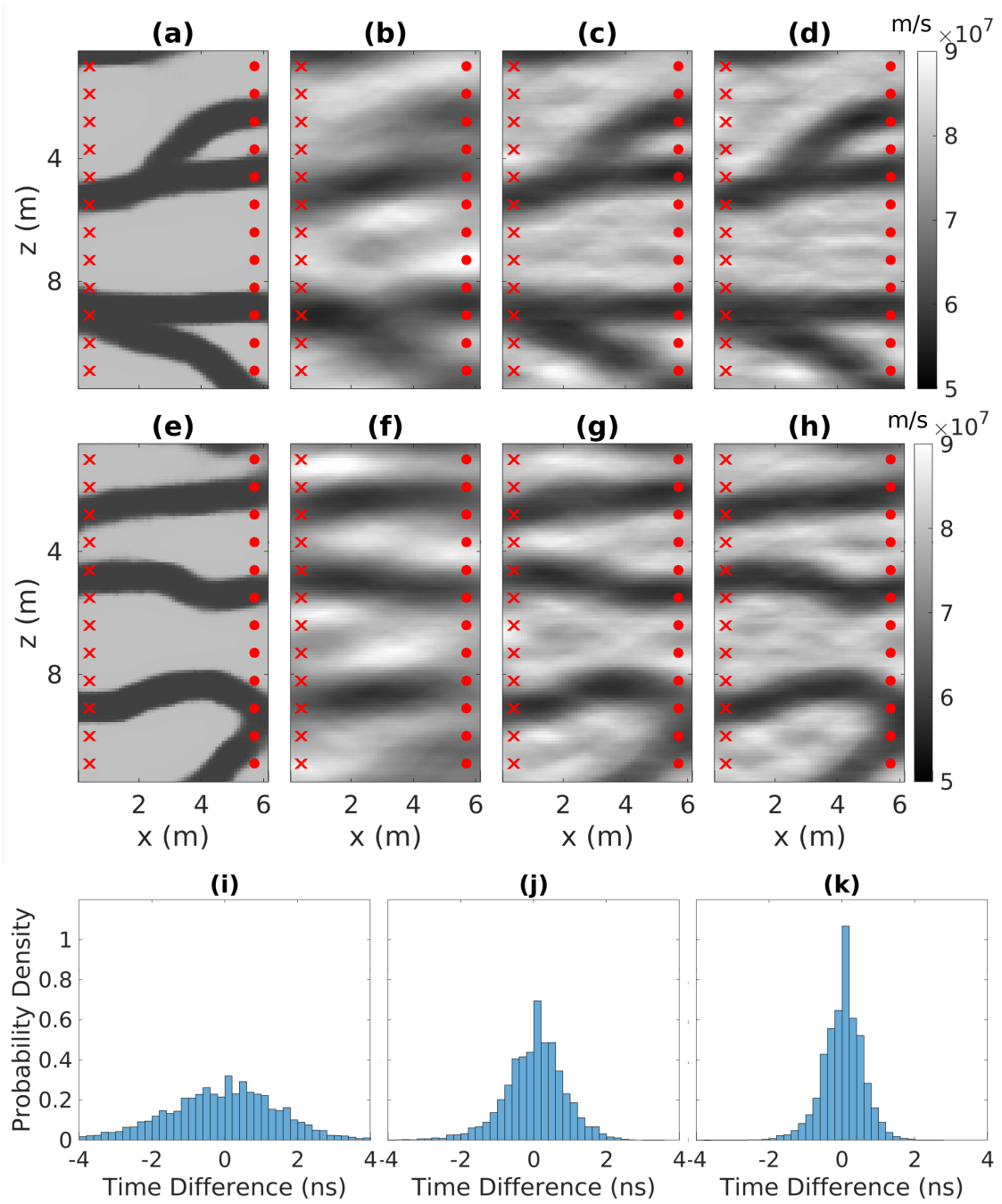


Figure 3: (a) and (e) Random velocity distributions and the corresponding representations using the first (b) and (f) 30, (c) and (g) 60, and (d) and (h) 90 principal components defined with the global approach; (i-k) corresponding histograms of travel-time residuals based on simulations on the true field and partial reconstructions for 100 velocity distributions. Crosses and circles stand for sources and receivers, respectively.

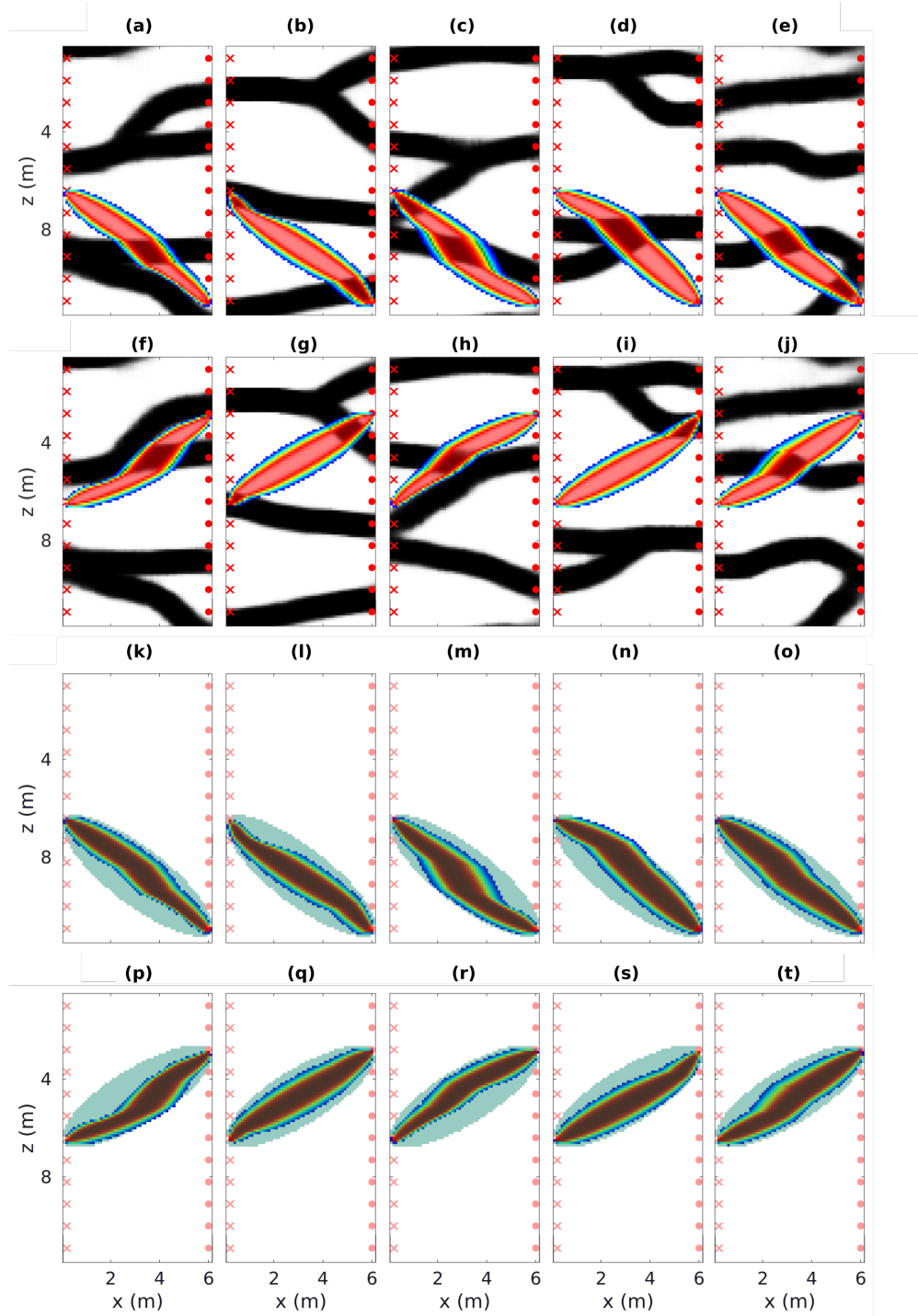


Figure 4: (a)-(j) For the distributions introduced in Fig. 1, the sensitivity-based kernels for two arbitrarily selected source/receiver pairs are shown superimposed on the corresponding velocity distributions. (k)-(t) The same sensitivity kernels as in (a)-(j), but superimposed on the cumulative kernels (green shaded areas) used to define the support of the sensitivity-based principal components used in the Local-PCA-PCE approach.

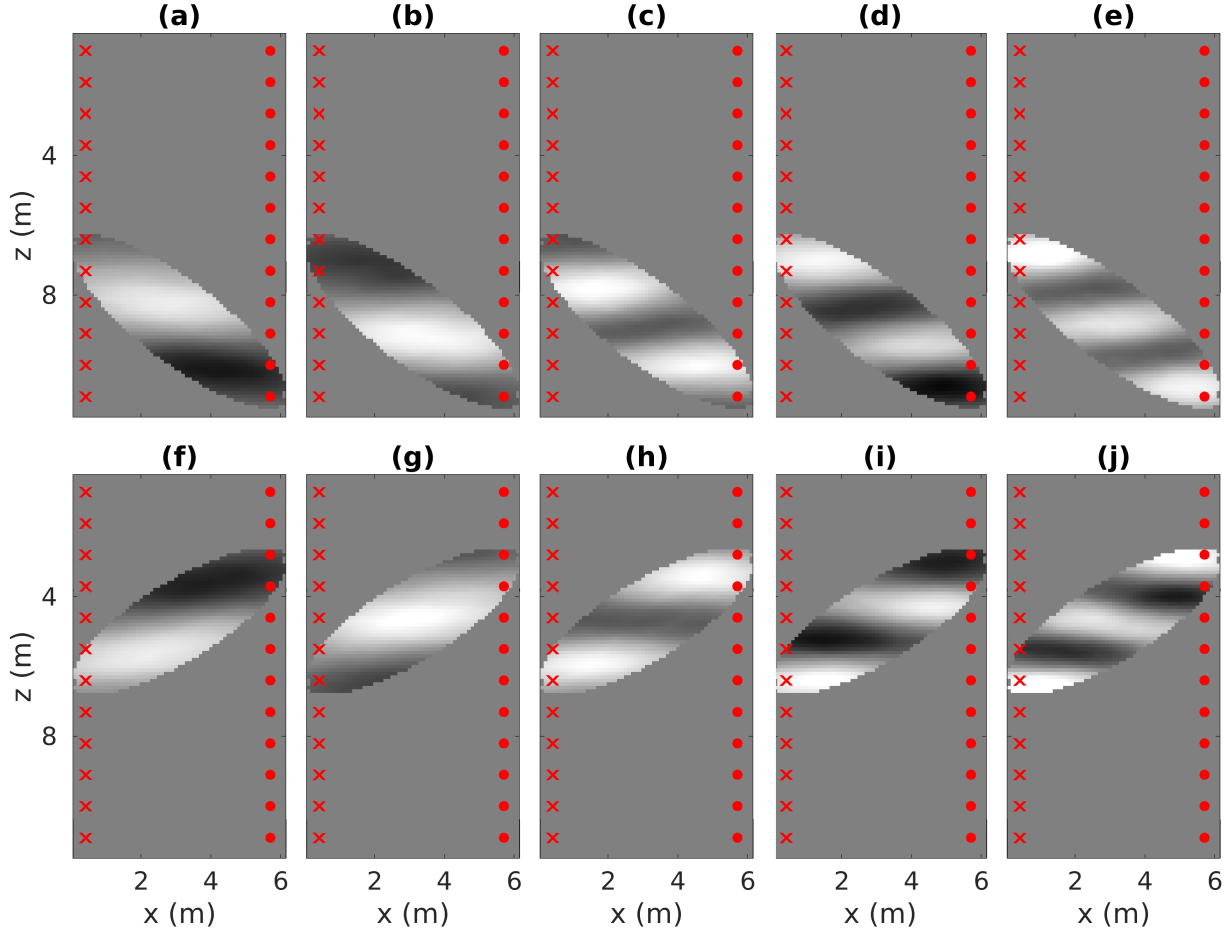


Figure 5: The first five principal components in the input domain corresponding to the cumulative kernels introduced in Fig. 4(k)-(t).

In Fig. 6(a)-(g) the two slowness distributions from Fig. 3 are shown next to the approximate representations obtained by projecting them on 30 local principal components defined specifically for different source-receiver angles. In the areas complementary to the sensitivity kernels, the speed is set to 0.07 m/ns. Input reconstructions are remarkably improved with respect to when using the same number of PCs (compare 6(a)-(g) and (h)-(l) to Fig. 3(b) and (f) of the entire slowness field). More interestingly, the modeling errors provided by using just 30 sensitivity-based PCs is lower than what was previously provided by 90 standard components (i.e., $\text{rms} \approx 0.45$ ns). These considerations underscore the significance of introducing a new category of PCs that are driven by the forward model. By incorporating these tailored PCs, we can attain enhanced output fidelity when utilizing truncated representations of the input. This enhanced fidelity proves particularly advantageous for the implementation of PCE, allowing for more precise and efficient modeling of intricate systems. Consequently, this approach holds substantial promise in achieving superior accuracy and computational efficiency in PCE-based analyses.

We have introduced three different parametrizations to be used for PCE. We consider coordinates inherited by the VAE, and principal components derived by considering either entire slowness fields or sensitivity-based sub-domains. We refer to these three parametrizations in what follows as VAE-PCE, Global-PCA-PCE and Local-PCA-PCE, respectively.

4.3 PCE performance

We here analyze the PCE performance of the different parametrizations for surrogate modeling introduced in Section 4.2. In agreement with Meles et al. (2022), we consider for each surrogate a total of 900 training sets and a polynomial degree p of five, for all three schemes when applied on eikonal data.

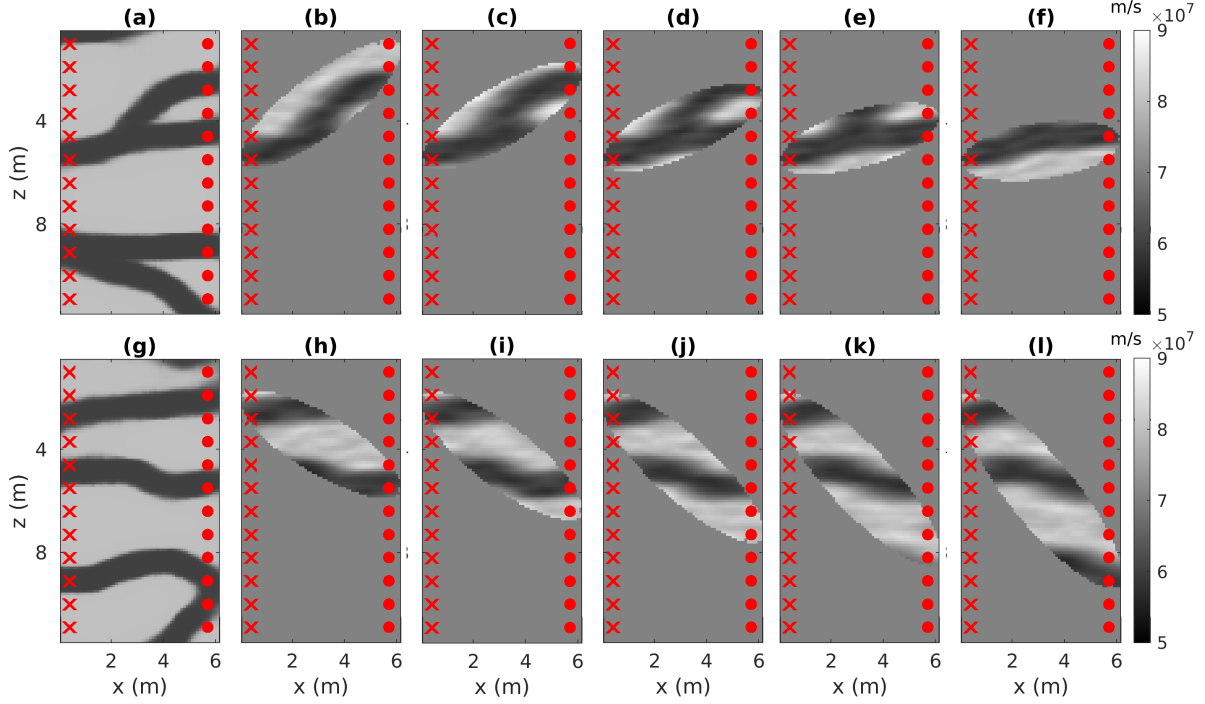


Figure 6: (a) and (g) Velocity distributions with (b)-(f) and (h)-(l) the corresponding representations used for surrogate modeling based on the first 30 principal components used in the Local-PCA-PCE approach. Different kernels are used for each source/receiver angle.

When the VAE parametrization is used as input, the PCE performance is rather poor, with a rmse of 2.01 ns, which is well beyond the noise level and consequently considered unsatisfactory. (see Fig. 7). The poor performance is due to the highly non-linear map \mathcal{N}_{VAE} . In such a scenario, PCE does not provide accurate results even if the physical input of the validation set is exactly defined by the deep generative network $\mathcal{G}_{VAE}(z) = \mathbf{u}$. In this scheme, note that the evaluation of $\mathcal{G}_{VAE}(z)$ is not required to compute the corresponding PCE.

Despite the partial reconstruction of the input ($\mathcal{G}_{PCA}(\mathbf{x}) \approx \mathbf{u}$) provided by the PCA approaches, the corresponding parametrizations provide good results when used to build PCE surrogates, with the Global-PCA-PCE approach being outperformed by the Local-PCA-PCE scheme in terms of accuracy (rmse of 1.31 and 0.68 ns, respectively, see Fig. 7(b) and (c) for the corresponding histograms). In both cases, the PCE operates on more variables (i.e., 60 and 30 for the Global-PCA-PCE and Local-PCA-PCE parametrizations, respectively, versus 20 for the VAE-PCE scheme). Moreover, the input for the Global-PCA-PCE and Local-PCA-PCE schemes are projections of images, which require the evaluation of $\mathcal{G}_{VAE}(z)$, on PCs. As such, evaluation of the corresponding PCEs is computationally more expensive for the PCA-based approaches than for the VAE-PCE case. In the Local-PCA-PCE approach, for each of the 23 angles considered, training involves randomly chosen source/receiver- pair data associated with identical altitude differences, while the final rmse is computed on the standard 144 travel-time gathers. For the Local-PCA-PCE scheme we also consider training and validation using FDTD data in addition to the eikonal data discussed above. Results are similar and still well below the noise, with an rmse of 0.65 ns (the corresponding histogram is displayed in Fig. 7(d)). All PCE results are unbiased and closely resemble Gaussian distributions.

Depending on the parameterization chosen, PCEs approximate eikonal and FDTD solvers to different degrees. Figure 8 represent the corresponding covariance matrices accounting for the modeling error of each surrogate model. A graphical summary of the proposed parameterizations of the PCE input variables introduced in Section 2 is depicted in Fig. 9.

Despite excellent input representation, PCE performance associated with the VAE parametrization are poor (left column), regardless of the maximum degree used (here we consider a maximum degree of five, as indicated by $\alpha \in \mathbb{N}_5^{20}$). The family of orthonormal polynomials, Ψ , are entirely determined by the statistical properties of z and do not depend on the source-receiver pair, whereas the coefficients $a_{\alpha}^{s,r}$ obviously do. Things improve when the Global-PCA-PCE strategy is used. Also in this case we consider a maximum degree of five (indicated by $\alpha \in \mathbb{N}_5^{60}$ since we have 60 parameters). Once again, the family of orthonormal polynomials Ψ^{gl} (which are constructed on the global principal

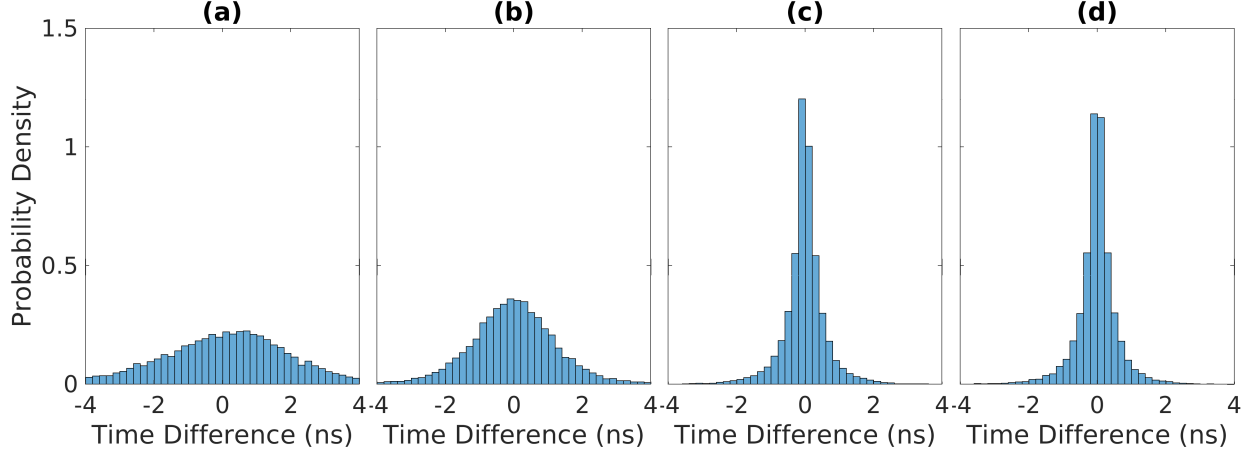


Figure 7: (a)-(c): Histograms of the model error with respect to the PCE prediction when using the VAE, Global and Local parameterizations of the input in the PCE-based surrogate modeling, respectively, using the eikonal solver to compute the training set. (d) Histogram of the model error using Local parameters and FDTD reference data.

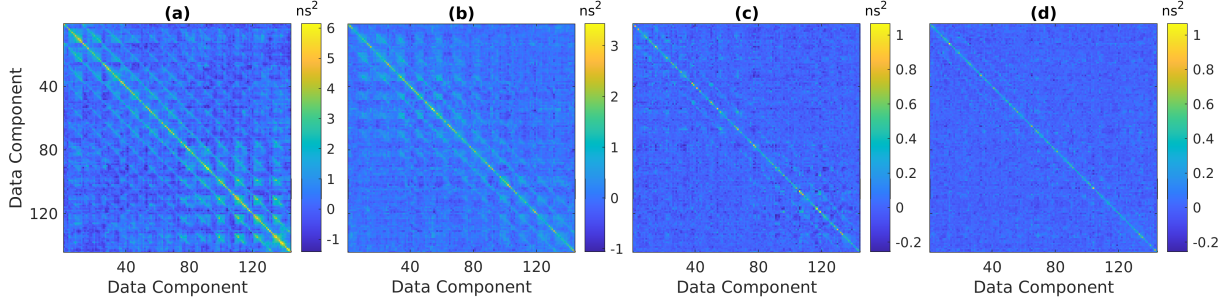


Figure 8: Model error covariance matrices associated with PCE-based surrogate modeling based on: (a) VAE-PCE, (b) Global-PCA-PCE and (c) Local-PCA-PCE schemes trained with 900 eikonal datasets. (d) Model error covariance matrix for the Local-PCA-PCE scheme trained with FDTD data.

components) do not depend on the source-receiver pair, while the (different) coefficients $a_{\alpha}^{s,r}$ do. By far, the best results are achieved when the Local-PCA-PCE strategy is chosen. In this case $\alpha \in \mathbb{N}_5^{30}$, however the family of orthonormal polynomials, Ψ^{θ} , depend on the angle between the source-receiver pair (upon which the local principal components are built), with multiple source/receiver pairs relying on the same polynomial bases, while the coefficient depend strictly on the source-receiver pair $a_{\alpha}^{s,r}$.

We now discuss the computational burden of each strategy when running on a workstation equipped with 16GB DDR4 of RAM and powered by a 3.5GHz Quad-Core processor running Matlab and Python on Linux. We emphasize that our goal with the present manuscript is to propose novel methods to conjugate VAE and PCE rather than offer optimized implementations.

There are up to three relevant computational steps in the execution of a forward run for the VAE-PCE, Global-PCA-PCE, Local-PCA-PCE, eikonal and FDTD simulations, namely the evaluation of the physical input, $\mathcal{G}_{VAE}(z)$, its decomposition on either global or local principal components and the actual evaluation of the forward model. Not all methods require each of these steps. The VAE-PCE model, for example, is not a function of $\mathcal{G}_{VAE}(z)$ but rather depends on z only. Evaluation of the VAE-PCE model is extremely fast both when involving one or 35 (as in the MCMC inversion discussed below, based on 35 chains) simultaneous model runs, taking on average ≈ 0.06 and $\approx 0.08s$, respectively. Evaluation of the Python-based decoder $\mathcal{G}_{VAE}(z)$, required for all forward models except the VAE-PCE, is actually the bottleneck of the Matlab algorithms used here, requiring ≈ 1.35 and $\approx 1.43s$, respectively, when operating on one or 35 input when considering the eikonal solver. However, this cost could be decreased with either an ad hoc implementation of the decoder or PCE in the same environment or with a more efficient calls of the Matlab/Python scripts in our codes. When in its native environment, evaluation of $\mathcal{G}_{VAE}(z)$ is actually very fast, taking only ≈ 0.005 and $\approx 0.08s$ when operating on one or 35 inputs, respectively. Still, note that this cost is overall negligible

Table 1: Summary of the computational cost of the various steps for a single realization/batch of 35 input of the proposed algorithms. In addition to the strategies used in the MCMC examples discussed in the manuscript and summarized in the first four columns (i.e., the VAE-PCE, Global- and Local-PCA-PCE and eikonal schemes), we also consider the cost of the FDTD approach using the reference code (fifth column) and an optimized Local-PCA-PCE approach ideally benefitting from executing the VAE decoder in the same environment as the PCE model and based on a single polynomial family for all angles (sixth column).

	VAE-PCE	Global-PCA-PCE	Local-PCA-PCE	eikonal	FDTD	Optimized Local-PCA-PCE
$\mathcal{G}_{VAE}(\mathbf{z})$	N/A	$\approx 1.35/1.43s$	$\approx 1.35/1.43s$	$\approx 1.35/1.43s$	$\approx 1.35/1.43s$	$\approx 0.005/0.08s$
PCA	N/A	$\approx 0.002/0.05s$	$\approx 0.06/0.23s$	N/A	N/A	$\approx 0.06/0.23s$
Forward	$\approx 0.06/0.08s$	$\approx 0.52/0.57s$	$\approx 0.64/0.65s$	$\approx 0.05/1.67s$	$\approx 120/4200s$	$\approx 0.06/0.16s$

even in our non-optimized setting when considering expensive physics-based forward solvers such as FDTD. Only the Global-PCA-PCE and Local-PCA-PCE strategies require PCA decompositions. The Global-PCA-PCE approach is faster, requiring only up to $\approx 0.002s$ and $\approx 0.05s$ when applied to one and 35 input elements, respectively, while the Local-PCA-PCE method is slower, taking up to $\approx 0.06s$ and $\approx 0.23s$ in the same situation. For the Global-PCA-PCE method the cost of a single forward run is $\approx 0.52s$, which is significantly more than for VAE-PCE. The difference between these two PCE strategies can be attributed to the significantly larger number of input parameters of the Global-PCA-PCE with respect to the VAE-PCE scheme (i.e., 60 vs 20). Note that the PCE model evaluations are vectorized and, therefore, the cost is almost the same when applied to 35 input ($\approx 0.57s$). Moreover, the computational cost of the Global-PCA-PCE method could be reduced by applying a PCA decomposition of the output, akin to what is proposed in Meles et al. (2022). Despite involving fewer variables than the Global-PCA-PCE approach, the Local-PCA-PCE method is slightly more computationally demanding with a cost of $\approx 0.64s$ and $\approx 0.65s$, respectively, when operating on one or 35 input, respectively. The increase in cost compared to the Global-PCA-PCE method depends on the fact that each Local-PCA-PCE has its own family of polynomials Ψ^θ (see 9). Differently than PCE methods, the cost of the reference eikonal solver is basically a linear function of the number of input distributions it operates on. A single run requires $\approx 0.05s$, while given 35 velocity distributions the cost increases up to $\approx 1.67s$. As such, its cost are either significantly smaller or slightly larger than what required by the Global/Local-PCA-PCE approaches. Finally, the cost required by the reference FDTD code is $\approx 120s$ and $\approx 4200s$ if operating on either one or 35 velocity distributions, which is orders of magnitude longer than for the eikonal or PCE models. These results are summarized in Table 1, where we estimate the performance of an ideally-optimized Local-PCA-PCE method benefitting from (a) evaluating $\mathcal{G}_{VAE}(\mathbf{z})$ in its native environment and (b) using a single family of polynomials Ψ^θ for all angles. In numerical results not presented herein, we find that choosing *any one* of the Ψ^θ families for all models provides nearly identical fidelity to what is achieved by using specifically tailored polynomials for each angle at the considerably smaller cost of ≈ 0.06 and $0.16s$ when applied to either one or 35 input, respectively. While such a result cannot be generalized, it is always possible to test the corresponding PCEs accuracy with a representative evaluation set. The option of relying on a single family of polynomials for the Local-PCA-PCE method is certainly to be taken into account when computationally-optimising algorithms.

4.4 Inversion results

We now explore the performance of the different parametrizations used for PCE-based surrogate modeling, namely VAE-PCE, Global-PCA-PCE and Local-PCA-PCE, when performing probabilistic MCMC inversion. The inversions were carried out using the UQLAB Matlab-based framework (Marelli and Sudret, 2014; Wagner et al., 2021b). We invert for the slowness distribution shown in Fig. 10, which is used to generate a total of 144 travel-times using the reference eikonal and FDTD solvers. Note that this slowness field is not used to train the PCEs. Uncorrelated Gaussian noise characterized by $\sigma^2 = 1ns^2$ was added to the data used for inversion.

We use a Metropolis-Hastings algorithm, and run 35 Markov chains in parallel for 4×10^5 iterations. A burn-in period defined according to the Geweke method prevents over-sampling regions around starting points, while the scaling factor of the proposal distribution is tuned so that an acceptance rate of about 30% is achieved for each experiment (Geweke, 1992; Brunetti et al., 2019). Finally, outlier chains with respect to the Inter Quartile-Range statistics discussed in Vrugt et al. (2009) are considered aberrant trajectories and are ignored in the MCMC analysis.

We first present the results for training data generated by an eikonal solver. We compare VAE-PCE, Global-PCA-PCE and Local-PCA-PCE inversion results to those achieved by employing the eikonal solver, which represent the reference solution since the full physics solver is used in the entire MCMC process. Inversion results in terms of mean and standard deviations incorporating the model error (i.e. using PCE derived \mathcal{C}_{Tapp} and \mathbf{d}_d in Eqs. (9) and (11), respectively) are

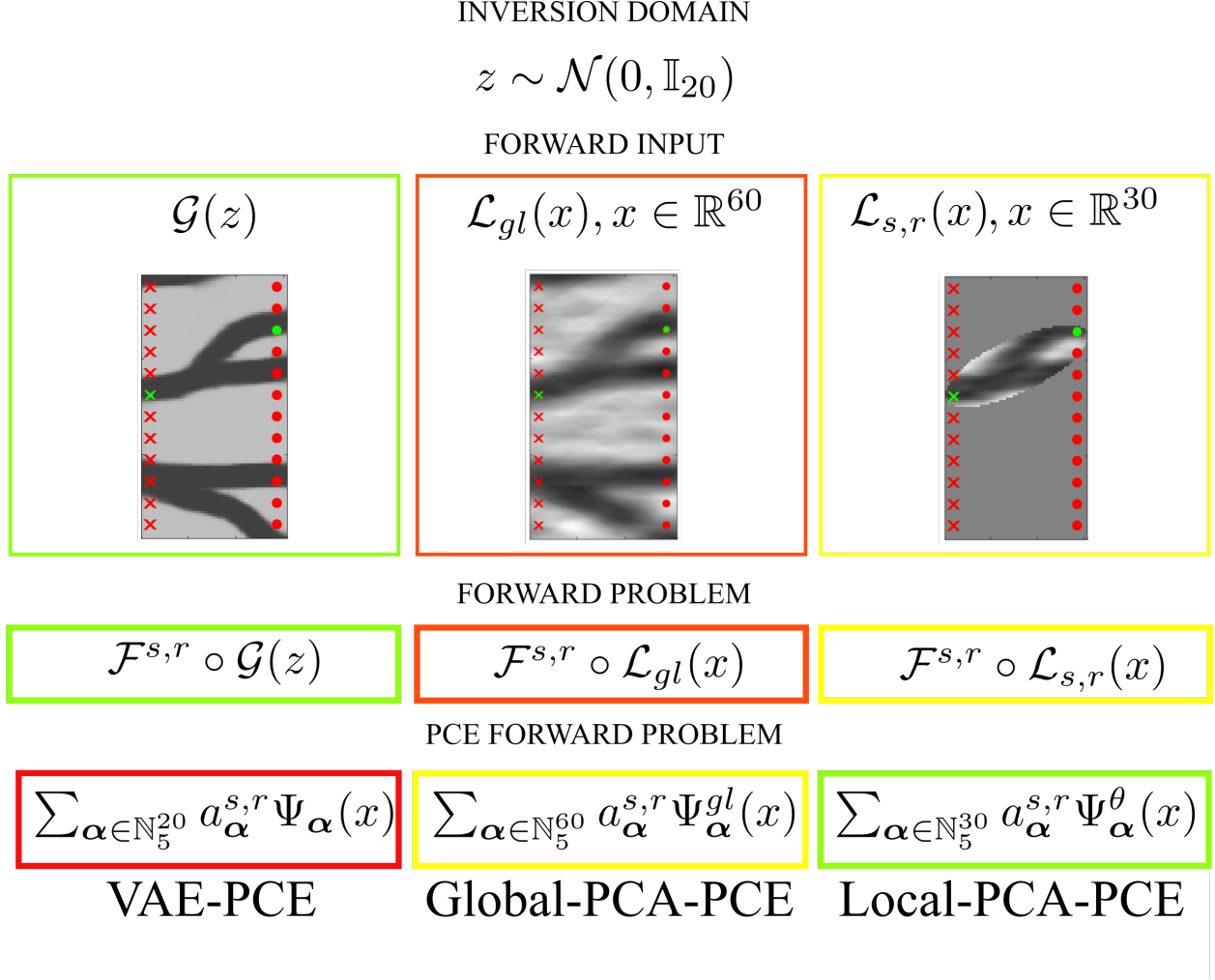


Figure 9: Graphical summary of the three strategies discussed in this manuscript. The prior distribution is always parametrized by the latent space of the VAE, with $z \sim \mathcal{N}(0, \mathbb{I}_{20})$, while the input to the PCE surrogate modeling depends on the chosen strategy. When the VAE parametrization is chosen, draws of the latent variables are considered (left column). With the PCA-PCE strategies, 60 globally or 30 locally defined PCs are used for the Global and Local approach, respectively (central and right column). The green, yellow and red boxes indicate various degrees of fidelity of the represented function, from best to worst, while the green cross and circle stand for a source-receiver whose forward problem we focus on. Fidelity in the reconstruction of the forward input turns into fidelity of the reference forward problem. However, PCE performance associated with the VAE parametrization are poor (left column). Things improve when the Global-PCA-PCE strategy is used, but by far, the best results are achieved when the Local-PCA-PCE strategy is chosen.

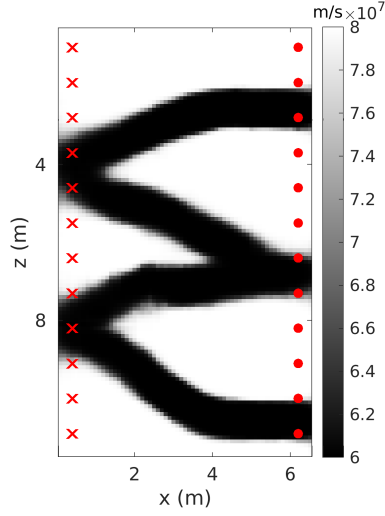


Figure 10: The reference velocity distribution used in the numerical inversion experiments.

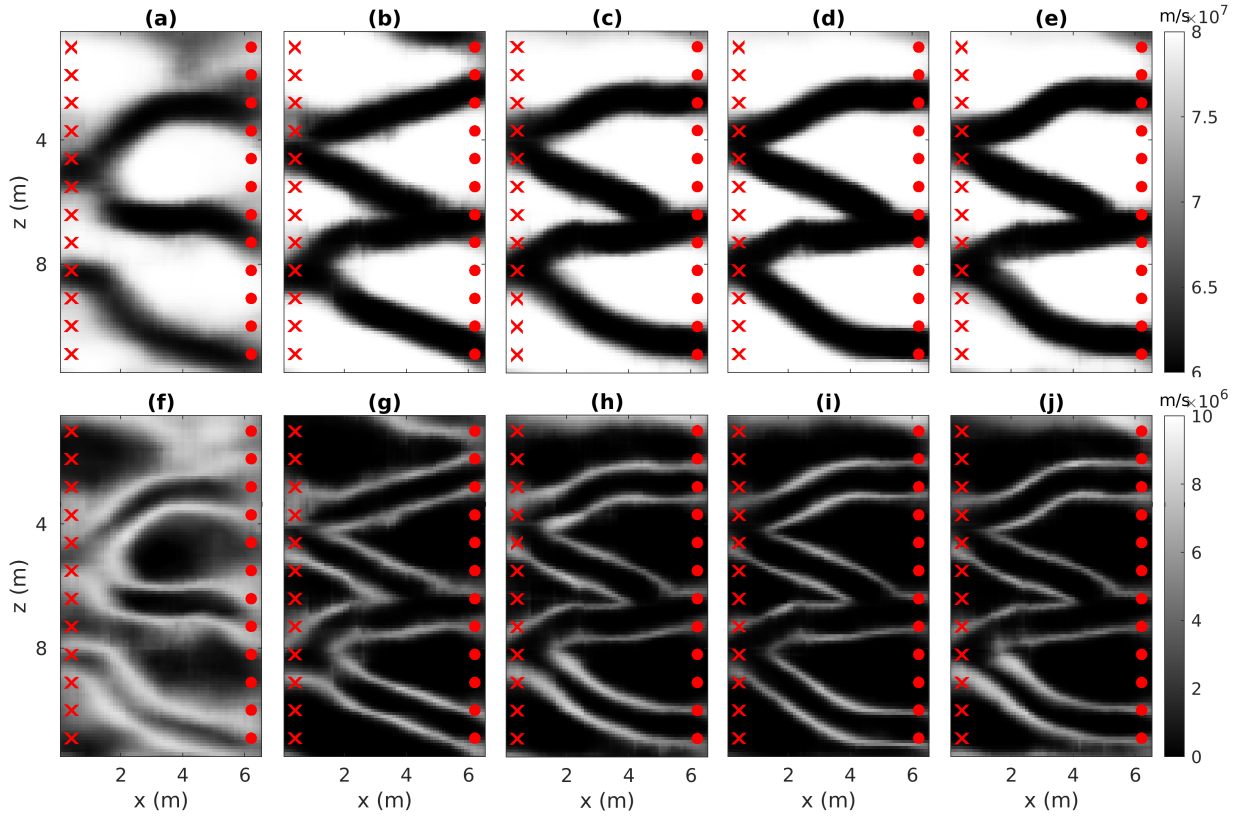


Figure 11: (a) Posterior mean and (f) standard deviation for the VAE-PCE inversion scheme. As for (a) and (f), but for the (b) and (g) Global-PCA-PCE, (c) and (h) Local-PCA-PCE, (d) and (i) eikonal and (e) and (j) FDTD Local-PCA-PCE inversion strategies, respectively.

Table 2: Assessment of the inversion results in the input and output domains for the various surrogate modeling strategies.

Model	RMSE Mean Velocity	SSIM Mean Velocity	rmse Mean Output
VAE-PCE	$8.01 \cdot 10^6$ m/s	0.30	3.49 ns
Global-PCA-PCE	$5.38 \cdot 10^6$ m/s	0.54	1.49 ns
Local-PCA-PCE	$2.67 \cdot 10^6$ m/s	0.73	1.15 ns
eikonal	$1.57 \cdot 10^6$ m/s	0.87	1.01 ns
FD Local-PCA-PCE	$3.06 \cdot 10^6$ m/s	0.71	1.15 ns

shown in Fig. 11(a-e). The mean of the posterior obtained employing the VAE-PCE poorly resembles the reference velocity field, with relevant topological differences between the two (compare Fig. 10 to Fig. 11(a)). Note that the misfit between the observed data used for inversion and the VAE-PCE evaluated on the reference input is particularly large for this input (i.e., 3.1 ns). This poor performance is also obtained when considering other test models (see Appendix A). The mean of the posterior provided by the Global-PCA-PCE approach shares many features with the reference distribution, but the two images visibly differ in the profile of the lower and upper channelized structures. The similarity between the posterior mean and the true distribution increases significantly when the Local-PCA-PCE is used (compare Fig. 10 to Fig. 11(c)). These results also show close proximity with the posterior mean solution obtained by the eikonal solver (see Fig. 11(d)), that is, without any surrogate modeling. Also, when the FDTD Local-PCA-PCE is employed, an almost identical solution to what is achieved using the Local-PCA-PCE is obtained (see Fig. 11(e)). For this alternative data set, the use of the FDTD solver in the inversion algorithm would be extremely expensive and is not considered here. The quality of the solution offered by the surrogate on FDTD data can be heuristically appreciated by noting its similarity to results obtained by the Local-PCA-PCE based on eikonal data, which in turn produces results close to those of the eikonal solver on eikonal data. Although not strictly consequential, it is then to be expected that the results offered by the surrogate-based on FD data would also be similar to those that would have been obtained if using the FDTD solver on FDTD data.

High standard deviations values are found distributed in wide domains of the image when VAE-PCE is used (see Fig. 11f). In contrast, when Global-PCA-PCE (Fig. 11g), Local-PCA-PCE (Fig. 11h) and eikonal (Fig. 11i) solvers are used, high standard deviation values are found mainly only along channel boundaries. Convergence is assessed using the potential-scale reduction factor \hat{R} considering the variance of the individual Markov chains with the variance of all the Markov chains merged together (Gelman and Rubin, 1992), as calculated by the second half of the chains. Convergence is usually assumed if $R < 1.2$ for all parameters. In our experiments, full convergence for all of the 20 parameters is achieved when the VAE-PCE, the Global-PCA-PCE and the Local-PCA-PCE approaches are used. Six parameters do not converge when the eikonal solver is employed, but the values R are nevertheless close to 1.2 (see Fig. 12). Further quantitative assessments can be achieved by comparing the reference input and the corresponding inversion solutions in terms of input domain root-mean-square error (in the following, RMSE), structural similarity (in the following, SSIM) and rmse in the output domain (Gneiting and Raftery, 2007; Levy et al., 2022a). Among these metrics, SSIM specifically evaluates the structural similarity between images, emphasizing their underlying patterns and details. It assigns a value between 0 and 1, with 0 indicating a notable dissimilarity and 1 denoting a substantial level of similarity. Again, we see that the VAE-PCE performs poorly, with a low SSIM (0.30) value and large input and output root-mean-square error ($8.01 \cdot 10^6$ m/s and 3.49 ns, respectively). Better results are provided by the Global-PCA-PCE strategy (SSIM, RMSE and rmse are 0.54 and $5.38 \cdot 10^6$ m/s and 1.49 ns, respectively). The Local-PCA-PCE scheme results are the closest to the reference solutions achieved using the eikonal solver (the corresponding SSIM, RMSE and rmse are 0.73 and 0.87, $2.67 \cdot 10^6$ m/s and $1.57 \cdot 10^6$ m/s and 1.15 and 1.01 ns, respectively). Also considering these additional metrics, the FDTD Local-PCA-PCE performs similarly to the Local-PCA-PCE strategy (SSIM: 0.71, RMSE: $3.06 \cdot 10^6$). The results are summarized in Table 2.

We also consider histograms of SSIM values in the posterior distributions provided by the five inversion schemes considered above. Fig. 13 shows how the VAE-PCE posterior has low similarity with the reference model, with the maximum SSIM value being below 0.5. Closer proximity is found among samples obtained using the Global-PCA-PCE approach, a trend that is further improved when considering the the Local-PCA-PCE scheme that shows some overlap with the results of the reference eikonal inversion. Note again that the FDTD Local-PCA-PCE algorithm is similar to the Local-PCA-PCE scheme, and thus the eikonal-based strategy, in this analysis as well. This can be further appreciated by looking at random posterior realizations for each of the inversion strategies discussed above (see Fig. 14).

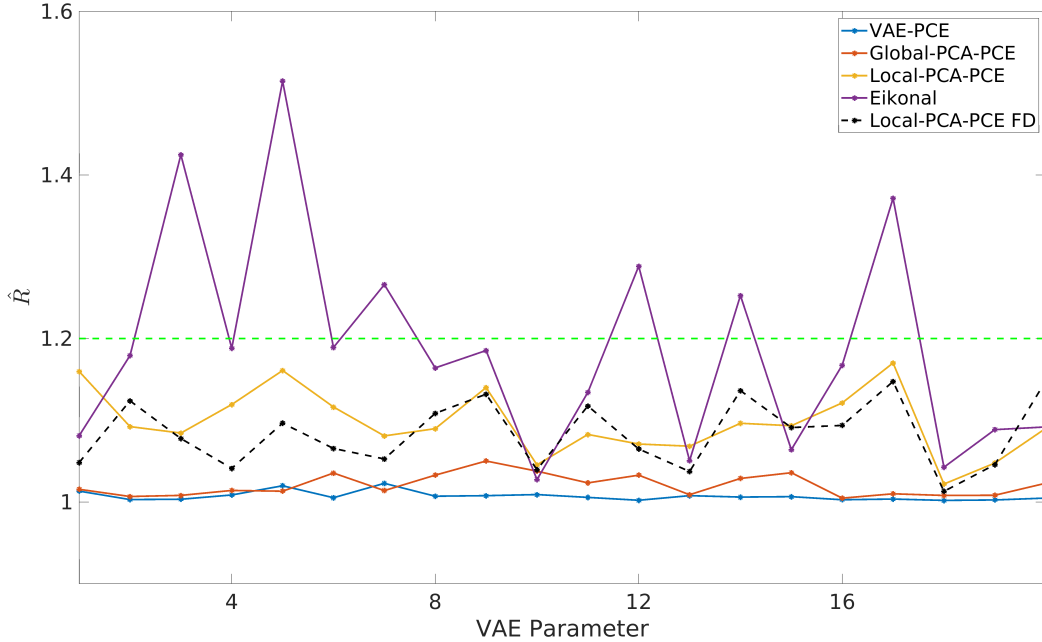


Figure 12: Gelman-Rubin statistics for the various inversion strategies.

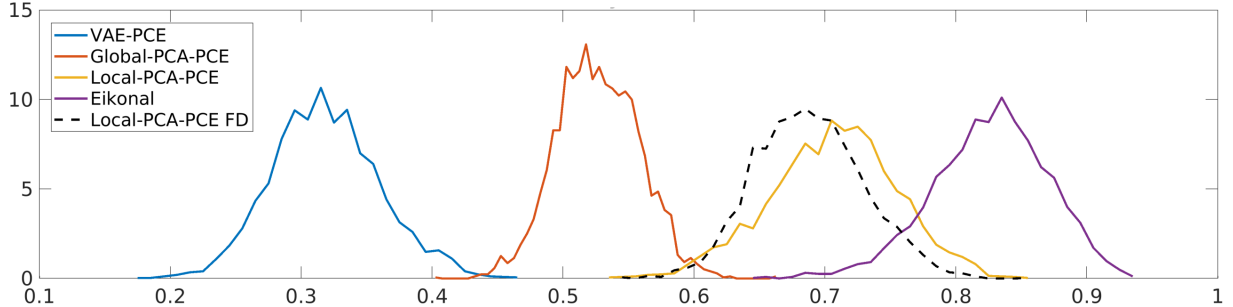


Figure 13: Histograms of SSIM values across the posterior distributions for the various inversion strategies.

5 Discussion

Deep generative networks, like VAEs, offer a robust framework for characterizing complex priors, enabling the description of intricate input distributions. However, proper characterization of prior distributions alone does not ensure the efficient estimation of posterior distributions when using MCMC methods. In such situations, the use of surrogate models becomes beneficial or even essential for evaluating likelihoods effectively. Surrogate modeling with PCE has become widespread in many disciplines. The massive decrease of the computational costs associated with PCE is achieved by approximating demanding computational forward models with simple and easy-to-evaluate functions. A key requirement to allow implementation of PCE is that the number of input variables describing the computational model is relatively small (i.e., up to a few tens) and that the target model can be approximated by truncated series of low-degree multivariate polynomials. The number of coefficients defining the PCE model grows polynomially in both the size of the input and the maximum degree of the expansion. When the reference full-physics model response is highly nonlinear in its input parameters, the problem is typically non-tractable (Torre et al., 2019). Since the high-fidelity mapping of complex prior distributions provided by deep generative networks is based on highly non-linear relationships between latent variables and physical domains, replicating the performance of such networks and/or composite functions thereof (e.g., $\mathcal{N}_{VAE} = \mathcal{F} \circ \mathcal{G}_{VAE}$ in Eq. 4) using PCE is problematic. To circumvent this challenge, we have explored two PCA-based decompositions that facilitated the straightforward implementation of

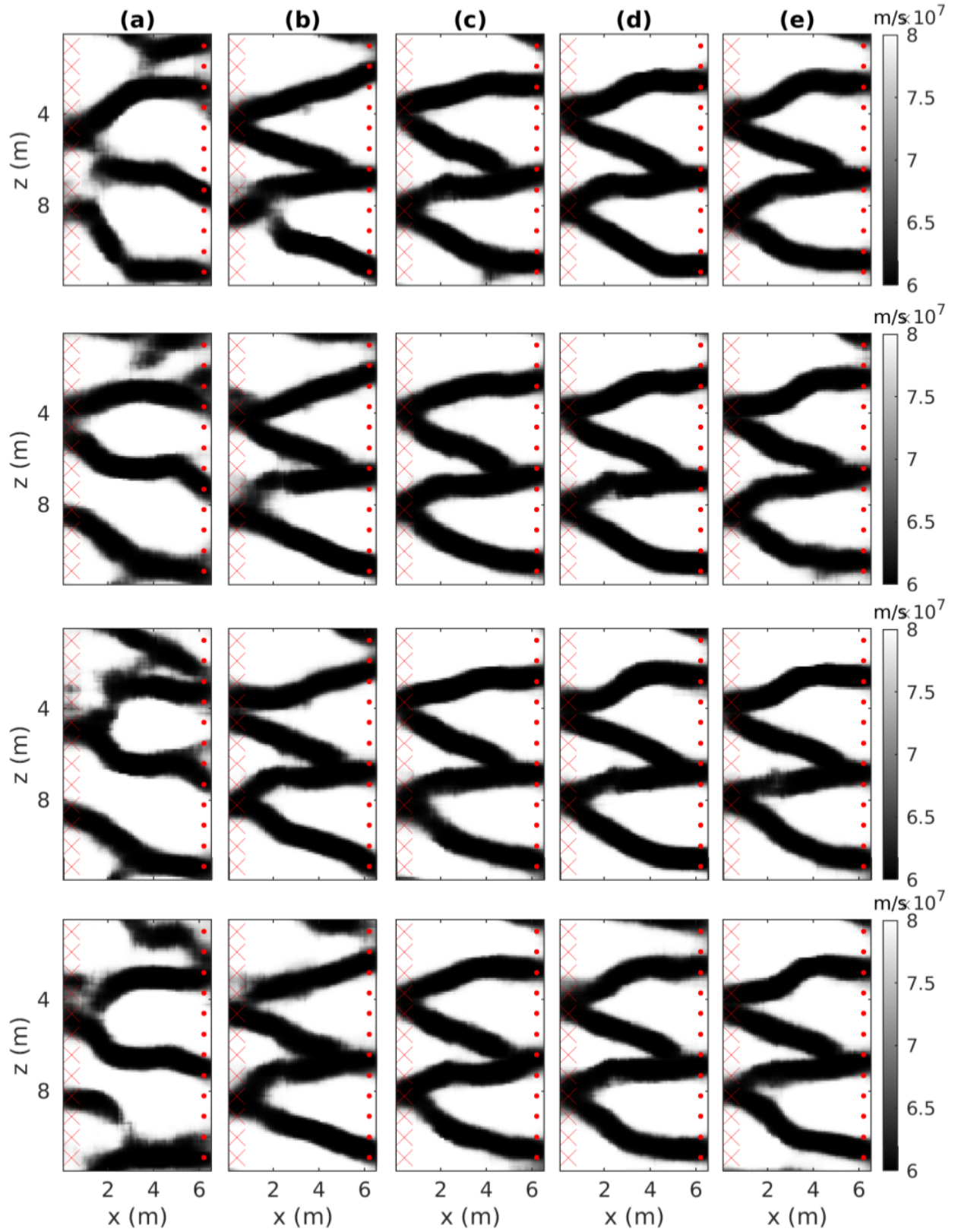


Figure 14: Random samples from the posterior obtained by employing the (a) VAE-PCE, (b) Global-PCA-PCE, (c) Local-PCA-PCE, (d) eikonal and (e) FD Local-PCA-PCE strategies. The results in c-e are visually similar.

PCE. One decomposition was designed to encompass the entire input domain, while the other specifically focused on subdomains of particular physical relevance within it. However, other potentially simpler parameterisations could have been considered, ideally not based on the analysis of a large sample of realisations of deep generative models but on properties of the input (including, for example, angle and mean/maximum/minimum velocity along the line connecting source and receiver or a sub-domain similar to the cumulative sensitivity kernels used here), which will be the subject of future research. Whatever the choice of input coordinates, for example, based on PCA or local properties of the input, the determining criterion for evaluating the quality of the corresponding PCE should always be performance on a representative validation set. In case of PCA, the lower bound of prediction misfit rmse can be a priori estimated by comparing the accuracy of the reference model acting on the full and the compressed domains, that is, $\mathcal{M}_{PCA}(x_{full})$ and $\mathcal{M}_{PCA}(x)$. In our case, such lower bounds for the Global-PCA-PCE approach operating with 60 components is 0.85 ns. Using the Local-PCA-PCE scheme with 30 components only, the rmse drops to 0.55 ns. However, the accuracy of the corresponding Global/LocalPCA-PCE is worse, with rmse of 1.31 and 0.67 ns, respectively, mainly due to the small size of the training set. Note that while the lower bound of PCA decreases when more PCs are taken into account, the corresponding accuracy of PCE is limited by the size of the training set. Increasing the number of components can actually worsen PCE performance if the training set is not adequate to determine the polynomial coefficients, which, as mentioned, grow significantly with input size. In our case, using 90 components would imply an rmse of 1.39 ns, which is worse than what was obtained by the 60 components PCE. Note that while for the VAE-PCE method the parametrization is inherited by the latent space structure, for the Global/Local-PCA-PCE schemes the number of variables/PCs has to be chosen based on accuracy and computational burden analysis, with the computational cost increasing with the size of the input. In this study using 30 components for both the Global-PCA-PCE and the Local-PCA-PCE strategies would have reduced the accuracy of the Global-PCA-PCE method. On the other hand, using 60 components for the Local-PCA-PCE scheme would have decreased the computational efficiency.

Both the VAE-PCE and Global-PCA-PCE consist of 144 (i.e., the total number of source/receiver combinations) different PCE models operating, for each travel-time simulation, on an identical input, that is, the latent variables or the 60 PCs characterizing the entire physical domain. On the other hand, the Local-PCA-PCE scheme consists of 23 (i.e., the total number of source/receiver altitude angles) different models operating, for each travel-time simulation, on 144 different input, that is, the 30 PCs characterizing each local sub-domain. Since each of the 23 models operates on specific local PCs, the corresponding families of orthonormal polynomials Ψ^θ are different. This is in contrast with the Global-PCA-PCE method, for which each model operates via a single family of polynomials, namely Ψ^{gl} . Thus, the Local-PCA-PCE scheme is computationally more demanding than the Global-PCA-PCE (see Table 1). However, the use of a single family of polynomials can also be considered for the Local-PCA-PCE method, resulting in shorter run time. When considering computational performance, an optimal implementation of $\mathcal{G}_{VAE}(z)$ should also be sought.

We have seen that once a latent parametrization has been found to reduce the effective dimensionality of the input domain and, based on PCA decompositions, high fidelity PCEs have been trained, MCMC inversion can be efficiently implemented. Relying on PCE rather than advanced deep learning methods can be advantageous in terms of ease of implementation, as potentially complex training of a neural network is not needed. Many effective sampling methods, such as Adaptive Metropolis, Hamiltonian Monte Carlo, or the Affine Invariant Ensemble Algorithm (Duane et al., 1987; Haario et al., 2001; Goodman and Weare, 2010) could be easily used in our workflow, but in the current implementation we have used a standard Metropolis-Hastings sampling algorithm.

Even if we considered borehole GPR applications, adaptation of the relatively effective Global-PCA-PCE strategy presented here could be employed for other imaging problems such as active or passive seismic tomography at different scales (Bodin and Sambridge, 2009; Galetti et al., 2017). On the other hand, implementation of the Local-PCA-PCE schemes would depend on the properties of the corresponding sensitivity kernels, which would require more careful evaluation and problem-specific design.

6 Conclusions

Low-dimensional latent variables associated with deep generative networks, such as VAE, optimally conform to complex priors, and provide an ideal setting to explore posterior model distributions using MCMC strategies. MCMC methods can also benefit greatly from surrogate modeling based on PCE, provided the forward model can be approximated by low-degree multivariate polynomials. Such latent variable models tend to have a highly non-linear relation to data, and are, thus, poorly approximated by low-degree PCEs. As such, performing PCE-accelerated MCMC inversion based on a latent parametrization for both inversion and surrogate modeling leads to large posterior uncertainty due to the need to account for modeling errors in the likelihood function. Indeed, in the context of GPR travel-time tomography, PCE based on VAE latent variables results in modeling error well beyond noise level. By separating the parametrization used for inversion and the one for surrogate modeling, we can circumvent this problem and perform MCMC in a latent space while modeling is approximated by PCEs operating on globally or locally-defined principal

components. We find that both globally- and locally- defined PCEs largely outperform surrogate modeling based on VAE parametrizations. For the channelized structures of interest, modeling errors are comparable to the typical observational errors when PCE are based on globally defined principal components and significantly better performance can be achieved when locally defined principal components are taken into account, with errors typically well below the noise level. Generally speaking, using PCE significantly reduces the computational burden of MCMC, but it can be successfully employed to perform non-linear MCMC inversion only if the corresponding modeling error is not excessively large. In this manuscript we have shown how PCE based on VAE parametrizations performs poorly in MCMC inversion, whereas PCE based on globally and locally-defined principal components produce results comparable or close to those obtained using full-physics forward solvers. The methods presented herein are extendable to other problems involving wave-based physics of similar complexity.

7 Acknowledgments

We acknowledge the feedback Prof. Andrew Valentine (Durham University) and Dr. Robin Thibaut (Ghent University) in the preparation of this preprint. Niklas Linde, Macarena Amaya and Shiran Levy acknowledge support by the Swiss National Science Foundation (project number: 184574).

8 Data availability

The data underlying this article are available upon request to the corresponding author.

References

- Annan, A. P. (2005). GPR methods for hydrogeological studies. In *Hydrogeophysics*, pages 185–213. Springer.
- Arcone, S. A., Lawson, D. E., Delaney, A. J., Strasser, J. C., and Strasser, J. D. (1998). Ground-penetrating radar reflection profiling of groundwater and bedrock in an area of discontinuous permafrost. *Geophysics*, 63(5):1573–1584.
- Blatman, G. and Sudret, B. (2011). Adaptive sparse polynomial chaos expansion based on least angle regression. *Journal of Computational Physics*, 230(6):2345–2367.
- Bodin, T. and Sambridge, M. (2009). Seismic tomography with the reversible jump algorithm. *Geophysical Journal International*, 178(3):1411–1436.
- Boutsidis, C., Mahoney, M. W., and Drineas, P. (2008). Unsupervised feature selection for principal components analysis. In *Proceedings of the 14th ACM SIGKDD international conference on Knowledge discovery and data mining*, pages 61–69.
- Brunetti, C., Bianchi, M., Pirot, G., and Linde, N. (2019). Hydrogeological model selection among complex spatial priors. *Water Resources Research*, 55(8):6729–6753.
- Chen, Y., de Ridder, S. A., Rost, S., Guo, Z., Wu, X., and Chen, Y. (2022). Eikonal tomography with physics-informed neural networks: Rayleigh wave phase velocity in the northeastern margin of the Tibetan plateau. *Geophysical Research Letters*.
- Chipman, H., George, E. I., McCulloch, R. E., Clyde, M., Foster, D. P., and Stine, R. A. (2001). The practical implementation of Bayesian model selection. *Lecture Notes-Monograph Series*, pages 65–134.
- Cuomo, S., Di Cola, V. S., Giampaolo, F., Rozza, G., Raissi, M., and Piccialli, F. (2022). Scientific machine learning through physics-informed neural networks: Where we are and what’s next. *arXiv preprint arXiv:2201.05624*.
- Duane, S., Kennedy, A. D., Pendleton, B. J., and Roweth, D. (1987). Hybrid Monte Carlo. *Physics Letters B*, 195(2):216–222.
- Ernst, J. R., Maurer, H., Green, A. G., and Holliger, K. (2007). Full-waveform inversion of crosshole radar data based on 2-D finite-difference time-domain solutions of Maxwell’s equations. *IEEE Transactions on Geoscience and Remote Sensing*, 45(9):2807–2828.
- Galetti, E., Curtis, A., Baptie, B., Jenkins, D., and Nicolson, H. (2017). Transdimensional Love-wave tomography of the British Isles and shear-velocity structure of the East Irish Sea Basin from ambient-noise interferometry. *Geophysical Journal International*, 208(1):36–58.
- Gelman, A. and Rubin, D. B. (1992). Inference from iterative simulation using multiple sequences. *Statistical Science*, 7(4):457–472.

- Geweke, J. (1992). Evaluating the accuracy of sampling-based approaches to the calculations of posterior moments. *Bayesian Statistics*, 4:641–649.
- Giannakis, I., Giannopoulos, A., and Warren, C. (2019). A machine learning-based fast-forward solver for ground penetrating radar with application to full-waveform inversion. *IEEE Transactions on Geoscience and Remote Sensing*, 57(7):4417–4426.
- Giannakis, I., Giannopoulos, A., Warren, C., and Sofroniou, A. (2021). Fractal-constrained crosshole/borehole-to-surface full-waveform inversion for hydrogeological applications using ground-penetrating radar. *IEEE Transactions on Geoscience and Remote Sensing*.
- Gloaguen, E., Marcotte, D., Chouteau, M., and Perroud, H. (2005). Borehole radar velocity inversion using cokriging and cosimulation. *Journal of Applied Geophysics*, 57(4):242–259.
- Gneiting, T. and Raftery, A. E. (2007). Strictly proper scoring rules, prediction, and estimation. *Journal of the American Statistical Association*, 102(477):359–378.
- Goodfellow, I., Pouget-Abadie, J., Mirza, M., Xu, B., Warde-Farley, D., Ozair, S., Courville, A., and Bengio, Y. (2020). Generative adversarial networks. *Communications of the ACM*, 63(11):139–144.
- Goodman, J. and Weare, J. (2010). Ensemble samplers with affine invariance. *Communications in Applied Mathematics and Computational Science*, 5(1):65–80.
- Haario, H., Saksman, E., and Tamminen, J. (2001). An adaptive Metropolis algorithm. *Bernoulli*, pages 223–242.
- Hansen, T. M. and Cordua, K. S. (2017). Efficient monte carlo sampling of inverse problems using a neural network-based forward—applied to GPR crosshole traveltime inversion. *Geophysical Journal International*, 211(3):1524–1533.
- Hansen, T. M., Cordua, K. S., Jacobsen, B. H., and Mosegaard, K. (2014). Accounting for imperfect forward modeling in geophysical inverse problems—exemplified for crosshole tomography. *Geophysics*, 79(3):H1–H21.
- Hansen, T. M., Cordua, K. S., Looms, M. C., and Mosegaard, K. (2013). Sippi: A matlab toolbox for sampling the solution to inverse problems with complex prior information: Part 2—application to crosshole GPR tomography. *Computers & Geosciences*, 52:481–492.
- Hastings, W. K. (1970). Monte carlo sampling methods using markov chains and their applications. *Biometrika*, 57(1):97–109.
- Higdon, D., McDonnell, J. D., Schunck, N., Sarich, J., and Wild, S. M. (2015). A Bayesian approach for parameter estimation and prediction using a computationally intensive model. *Journal of Physics G: Nuclear and Particle Physics*, 42(3):034009.
- Holm-Jensen, T. and Hansen, T. M. (2020). Linear waveform tomography inversion using machine learning algorithms. *Mathematical Geosciences*, 52(1):31–51.
- Husen, S. and Kissling, E. (2001). Local earthquake tomography between rays and waves: fat ray tomography. *Physics of the Earth and Planetary Interiors*, 123(2-4):127–147.
- Irving, J. and Knight, R. (2006). Numerical modeling of ground-penetrating radar in 2-D using MATLAB. *Computers & Geosciences*, 32(9):1247–1258.
- Jensen, J. M., Jacobsen, B. H., and Christensen-Dalsgaard, J. (2000). Sensitivity kernels for time-distance inversion. *Solar Physics*, 192(1):231–239.
- Jetchev, N., Bergmann, U., and Vollgraf, R. (2016). Texture synthesis with spatial generative adversarial networks. *arXiv preprint arXiv:1611.08207*.
- Jolliffe, I. T. and Cadima, J. (2016). Principal component analysis: a review and recent developments. *Philosophical Transactions of the Royal Society A: Mathematical, Physical and Engineering Sciences*, 374(2065):20150202.
- Kingma, D. P. and Welling, M. (2013). Auto-encoding variational bayes. *arXiv preprint arXiv:1312.6114*.
- Klotzsche, A., Vereecken, H., and van der Kruk, J. (2019). Review of crosshole ground-penetrating radar full-waveform inversion of experimental data: Recent developments, challenges, and pitfalls. *Geophysics*, 84(6):H13–H28.
- Kuroda, S., Takeuchi, M., and Kim, H. J. (2007). Full-waveform inversion algorithm for interpreting crosshole radar data: a theoretical approach. *Geosciences Journal*, 11(3):211–217.
- LaBrecque, D., Alumbaugh, D. L., Yang, X., Paprocki, L., and Brainard, J. (2002). Three-dimensional monitoring of vadose zone infiltration using electrical resistivity tomography and cross-borehole ground-penetrating radar. In *Methods in Geochemistry and Geophysics*, volume 35, pages 259–272. Elsevier.

- Laloy, E., Héroult, R., Jacques, D., and Linde, N. (2018). Training-image based geostatistical inversion using a spatial generative adversarial neural network. *Water Resources Research*, 54(1):381–406.
- Laloy, E., Héroult, R., Lee, J., Jacques, D., and Linde, N. (2017). Inversion using a new low-dimensional representation of complex binary geological media based on a deep neural network. *Advances in Water Resources*, 110:387–405.
- Levy, S., Hunziker, J., Laloy, E., Irving, J., and Linde, N. (2022a). Using deep generative neural networks to account for model errors in markov chain monte carlo inversion. *Geophysical Journal International*, 228(2):1098–1118.
- Levy, S., Laloy, E., and Linde, N. (2022b). Variational bayesian inference with complex geostatistical priors using inverse autoregressive flows. *Computers & Geosciences*, page 105263.
- Lopez-Alvis, J., Laloy, E., Nguyen, F., and Hermans, T. (2021). Deep generative models in inversion: The impact of the generator’s nonlinearity and development of a new approach based on a variational autoencoder. *Computers & Geosciences*, 152:104762.
- Lüthen, N., Marelli, S., and Sudret, B. (2021a). Automatic selection of basis-adaptive sparse polynomial chaos expansions for engineering applications. *International Journal for Uncertainty Quantification*.
- Lüthen, N., Marelli, S., and Sudret, B. (2021b). Sparse polynomial chaos expansions: Literature survey and benchmark. *SIAM/ASA Journal on Uncertainty Quantification*, 9(2):593–649.
- Madsen, R. B. and Hansen, T. M. (2018). Estimation and accounting for the modeling error in probabilistic linearized amplitude variation with offset inversion. *Geophysics*, 83(2):N15–N30.
- Marelli, S., Lüthen, N., and Sudret, B. (2021). UQLab user manual – Polynomial chaos expansions. Technical report, Chair of Risk, Safety and Uncertainty Quantification, ETH Zurich, Switzerland. Report # UQLab-V1.4-104.
- Marelli, S. and Sudret, B. (2014). UQLab: A framework for uncertainty quantification in Matlab. In *Vulnerability, Uncertainty, and Risk (Proc. 2nd Int. Conf. on Vulnerability, Risk Analysis and Management (ICVRAM2014), Liverpool, United Kingdom)*, pages 2554–2563.
- Mariethoz, G. and Caers, J. (2014). *Multiple-point geostatistics: stochastic modeling with training images*. John Wiley & Sons.
- Marzouk, Y. and Xiu, D. (2009). A stochastic collocation approach to Bayesian inference in inverse problems. *Communications In Computational Physics*, 6.
- Marzouk, Y. M., Najm, H. N., and Rahn, L. A. (2007). Stochastic spectral methods for efficient Bayesian solution of inverse problems. *Journal of Computational Physics*, 224(2):560–586.
- Meles, G. A., Linde, N., and Marelli, S. (2022). Bayesian tomography with prior-knowledge-based parametrization and surrogate modeling. *Geophysical Journal International*.
- Meles, G. A., Van der Kruk, J., Greenhalgh, S. A., Ernst, J. R., Maurer, H., and Green, A. G. (2010). A new vector waveform inversion algorithm for simultaneous updating of conductivity and permittivity parameters from combination crosshole/borehole-to-surface GPR data. *IEEE Transactions on Geoscience and Remote Sensing*, 48(9):3391–3407.
- Métivier, D., Vuffray, M., and Misra, S. (2020). Efficient polynomial chaos expansion for uncertainty quantification in power systems. *Electric Power Systems Research*, 189:106791.
- Nagel, J. B. (2019). Bayesian techniques for inverse uncertainty quantification. *IBK Bericht*, 504.
- Olsson, O., Falk, L., Forslund, O., Lundmark, L., and Sandberg, E. (1992). Borehole radar applied to the characterization of hydraulically conductive fracture zones in crystalline rock. *Geophysical Prospecting*, 40(2):109–142.
- Raissi, M., Perdikaris, P., and Karniadakis, G. E. (2019). Physics-informed neural networks: A deep learning framework for solving forward and inverse problems involving nonlinear partial differential equations. *Journal of Computational Physics*, 378:686–707.
- Rawlinson, N., Sambridge, M., et al. (2003). Seismic travelttime tomography of the crust and lithosphere. *Advances in Geophysics*, 46:81–199.
- Reynolds, A. C., He, N., Chu, L., and Oliver, D. S. (1996). Reparameterization techniques for generating reservoir descriptions conditioned to variograms and well-test pressure data. *SPE Journal*, 1(04):413–426.
- Semenov, S. (2009). Microwave tomography: review of the progress towards clinical applications. *Philosophical Transactions of the Royal Society A: Mathematical, Physical and Engineering Sciences*, 367(1900):3021–3042.
- Smith, J. D., Azizzadenesheli, K., and Ross, Z. E. (2020). Eikonet: Solving the eikonal equation with deep neural networks. *IEEE Transactions on Geoscience and Remote Sensing*, 59(12):10685–10696.

- Sochala, P., Gesret, A., and Le Maitre, O. (2021). Polynomial surrogates for bayesian traveltime tomography. *GEM-International Journal on Geomathematics*, 12(1):1–34.
- Strebelle, S. (2002). Conditional simulation of complex geological structures using multiple-point statistics. *Mathematical Geology*, 34(1):1–21.
- Taillandier, C., Noble, M., Chauris, H., and Calandra, H. (2009). First-arrival traveltime tomography based on the adjoint-state method. *Geophysics*, 74(6):WCB1–WCB10.
- Tant, K. M. M., Galetti, E., Mulholland, A., Curtis, A., and Gachagan, A. (2018). A transdimensional Bayesian approach to ultrasonic travel-time tomography for non-destructive testing. *Inverse Problems*, 34(9):095002.
- Thibaut, R., Laloy, E., and Hermans, T. (2021). A new framework for experimental design using bayesian evidential learning: The case of wellhead protection area. *Journal of Hydrology*, 603:126903.
- Torre, E., Marelli, S., Embrechts, P., and Sudret, B. (2019). Data-driven polynomial chaos expansion for machine learning regression. *Journal of Computational Physics*, 388:601–623.
- Vecherin, S. N., Ostashev, V. E., Goedecke, G. H., Wilson, D. K., and Voronovich, A. G. (2006). Time-dependent stochastic inversion in acoustic travel-time tomography of the atmosphere. *The Journal of the Acoustical Society of America*, 119(5):2579–2588.
- Vrugt, J. A., Ter Braak, C., Diks, C., Robinson, B. A., Hyman, J. M., and Higdon, D. (2009). Accelerating markov chain monte carlo simulation by differential evolution with self-adaptive randomized subspace sampling. *International Journal of Nonlinear Sciences and Numerical Simulation*, 10(3):273–290.
- Wagner, P.-R., Fahrni, R., Klippel, M., Frangi, A., and Sudret, B. (2020). Bayesian calibration and sensitivity analysis of heat transfer models for fire insulation panels. *Engineering Structures*, 205:110063.
- Wagner, P.-R., Marelli, S., and Sudret, B. (2021a). Bayesian model inversion using stochastic spectral embedding. *Journal of Computational Physics*, 436:110141.
- Wagner, P.-R., Nagel, J., Marelli, S., and Sudret, B. (2021b). UQLab user manual – Bayesian inversion for model calibration and validation. Technical report, Chair of Risk, Safety and Uncertainty Quantification, ETH Zurich, Switzerland. Report UQLab-V1.4-113.
- Waheed, U. B., Alkhalifah, T., Haghightat, E., Song, C., and Virieux, J. (2021). Pinntomo: Seismic tomography using physics-informed neural networks. *arXiv preprint arXiv:2104.01588*.
- Wang, S., Teng, Y., and Perdikaris, P. (2021). Understanding and mitigating gradient flow pathologies in physics-informed neural networks. *SIAM Journal on Scientific Computing*, 43(5):A3055–A3081.
- Warren, C., Giannopoulos, A., Gray, A., Giannakis, I., Patterson, A., Wetter, L., and Hamrah, A. (2019). A CUDA-based GPU engine for gprMax: Open source FDTD electromagnetic simulation software. *Computer Physics Communications*, 237:208–218.
- Xiu, D. and Karniadakis, G. E. (2002). The Wiener-Askey polynomial chaos for stochastic differential equations. *SIAM Journal on Scientific Computing*, 24(2):619–644.
- Yu, J., Lu, L., Meng, X., and Karniadakis, G. E. (2022). Gradient-enhanced physics-informed neural networks for forward and inverse pde problems. *Computer Methods in Applied Mechanics and Engineering*, 393:114823.
- Zahner, T., Lochbühler, T., Mariethoz, G., and Linde, N. (2016). Image synthesis with graph cuts: a fast model proposal mechanism in probabilistic inversion. *Geophysical Journal International*, 204(2):1179–1190.

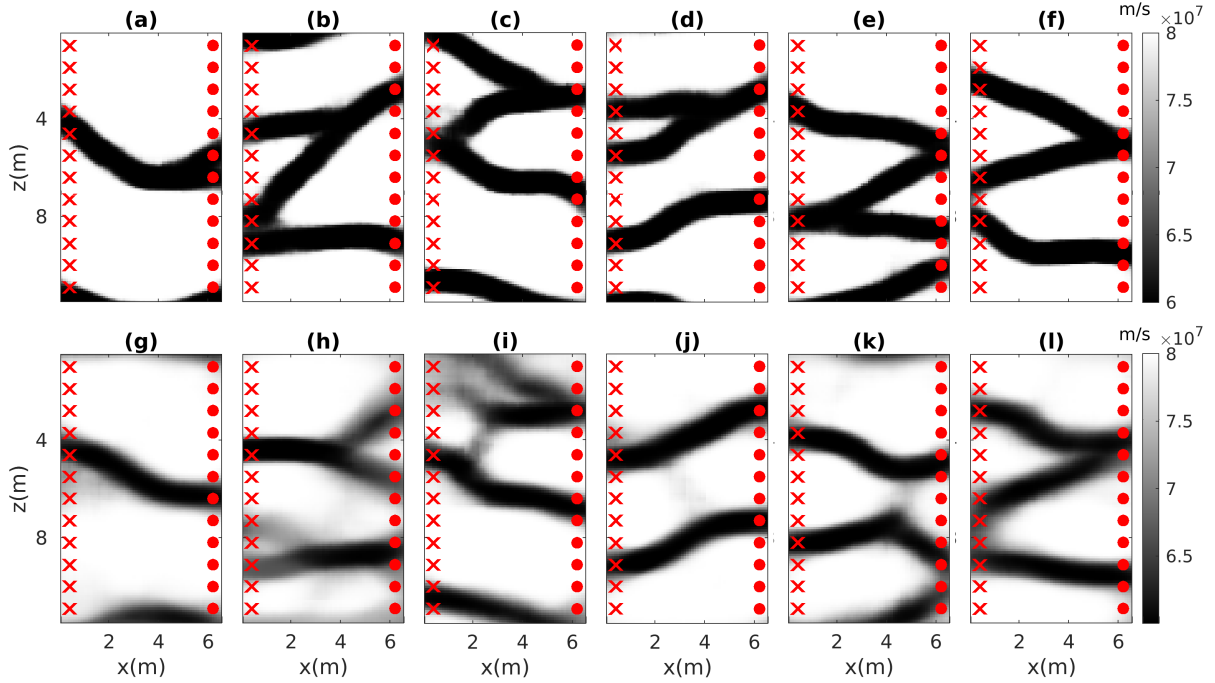


Figure A.1: Reference velocity fields (a)-(f) and (g)-(l) the corresponding posterior mean images for MCMC inversion based on VAE-PCE surrogate modeling.

A Appendix: overview of the limitations of the VAE-PCE approach

For the configuration considered in this manuscript, PCEs based on VAE parameters provide poor accuracy in predicting travel-times. When calculated on a representative validation set, an aggregate rmse of 2.01 ns is observed for the misfit between reference and predicted data. For the velocity distribution in Fig. 10, the travel-time prediction is particularly poor, with an rmse of 3.1 ns. In Fig. A.1, we consider six additional reference velocity fields and the corresponding posterior mean images for MCMC inversion when using VAE-PCE surrogate modeling. In some cases the posterior mean resembles the reference velocity field well (compare A.1(a) to A.1(g), or A.1(f) to A.1(l)). However, large differences can arise between the reference and the VAE-PCE posterior mean (e.g., compare A.1(b) to A.1(h), or A.1(e) to A.1(k)). Even if the corresponding modeling error is accounted for in the inversion implying that the posterior mean models should be unbiased, we find that the modeling error has severe impacts by increasing the posterior model uncertainty.